2009

Methods for iris classification and macro feature detection

Manisha Sam Sunder
West Virginia University

Methods for Iris Classification and Macro Feature Detection

by

Manisha Sam Sunder

Thesis submitted to the
College of Engineering and Mineral Resources
at West Virginia University
in partial fulfillment of the requirements
for the degree of

Master of Science
in
Electrical Engineering

Arun A. Ross, PhD., Chair
Xin Li, PhD.
Lawrence A. Hornak, PhD.

Lane Department of Computer Science and Electrical Engineering

Morgantown, West Virginia
2009

Keywords: Macro Features, Iris classification

Abstract

Methods for Iris Classification
and
Macro Feature Detection

by

Manisha Sam Sunder
Master of Science in Electrical Engineering

West Virginia University

Arun A. Ross, PhD., Chair

This work deals with two distinct aspects of iris-based biometric systems: iris classification and macro-feature detection. Iris classification will benefit identification systems where the query image has to be compared against all identities in the database. By pre-classifying the query image based on its texture, this comparison is executed only against those irises that are from the same class as the query image. In the proposed classification method, the normalized iris is tessellated into overlapping rectangular blocks and textural features are extracted from each block. A clustering scheme is used to generate multiple classes of irises based on the extracted features. A minimum distance classifier is then used to assign the query iris to a particular class. The use of multiple blocks with decision level fusion in the classification process is observed to enhance the accuracy of the method.

Most iris-based systems use the global and local texture information of the iris to perform matching. In order to exploit the anatomical structures within the iris during the matching stage, two methods to detect the macro-features of the iris in multi-spectral images are proposed. These macro-features typically correspond to "anomalies" in pigmentation and structure within the iris. The first method uses the edge-flow technique to localize these features. The second technique uses the SIFT (Scale Invariant Feature Transform) operator to detect discontinuities in the image. Preliminary results show that detection of these macro features is a difficult problem owing to the richness and variability in iris color and texture. Thus a large number of spurious features are detected by both the methods suggesting the need for designing more sophisticated algorithms. However the ability of the SIFT operator to match partial iris images is demonstrated thereby indicating the potential of this scheme to be used for macro-feature detection.

I dedicate my thesis to my family and friends

Acknowledgments

I would like to take this opportunity to thank Dr. Arun Ross my advisor and committee chair for giving me this opportunity to pursue my interest in the field of research. Without his guidance, motivation and insight it would not have been possible for me to understand the goal and the right aptitude towards research. The knowledge and experience gained during my work under Dr. Ross is a priced posession which has changed my perspective towards research and education.

I am thankful to Dr. Xin Li and Dr. Lawrence Hornak for their valuable suggestions and guidance. I am also thankful to all the faculty members of West Virginia University, from whom I have learnt and gained a lot knowledge and experience. I take this opportunity to express my happiness and gratitude to all my lab-mates Simona, Aglika, Rajiv, Nick, Dave, Chen, Eric, Asem, Ayman, Raghav and Brian for their help, suggestions and discussions. I would also like to thank Nikhil and other friends for their support, patience, encouragement and for making my stay at WVU and morgantown memorable. I want to express thanks to Mayank and Richa for their help and would also like to thank all my friends for their support and for always being there.

I am ever grateful to god for blessing me with a wonderful family for their support and love. I am thankful to my mother, the eternal pillar of strength, support and motivation, my dad for my source of inspiration to make use of resources available, grandfather for his guidance and advice, my brother for his bundle of energy, and Akshay for always being there. I thank them for their faith on me.

Without all of them this journey wouldnt have been possible for me. Each of them have an important role in making me what I am and bringing the best out of me. Thank you all.

Contents

List of Figures

Chapter 1

Introduction

1.1 Iris Introduction

1.1.1 Structure of the Human Eye

The human eye is divided into two chambers namely the anterior chamber and the posterior chamber [8]. Figure 1.1 shows the sagittal anatomy of the human eye. From the figure it is observed that posterior chamber lies behind the iris and in front of the lens and the anterior chamber is located behind the cornea. The posterior chamber is dark and is usually dark-brown in color. It contains the aqueous humor produced by the ciliary body located behind the iris, providing nutrients to the lens and cornea. This transparent fluid flows from the pupil to the anterior chamber. The anterior chamber is lightly colored due to the genetically determined density of melanin granules.

These two chambers are separated by the iris and the lens. The lens focuses the images on to the retina which is lined up with light receptors, namely the rod and cone cells, which are broadly responsible for perception of intensity and color, respectively. The iris is the colored part of the eye which is surrounded by the white sclera and the pupil. Figure 1.2 shows the sectional anatomy of the anterior iris.

The iris tissue is soft and is called the stroma. It is highly vascularized with interlacing ligaments containing melanocytes. The iris stroma is usually blue, hazel, green and brown in color based on the presence of melanin granules in the stroma. Blue irides contain the least number of melanosomes in the stromal melanocytes and the brown eyes contain the highest number of melanosomes in the melanocytes. The iris controls the amount

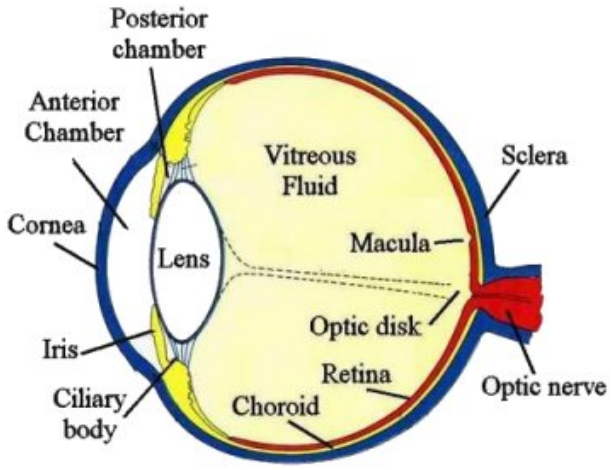

Figure 1.1: Sagittal section of the Human eye [1]

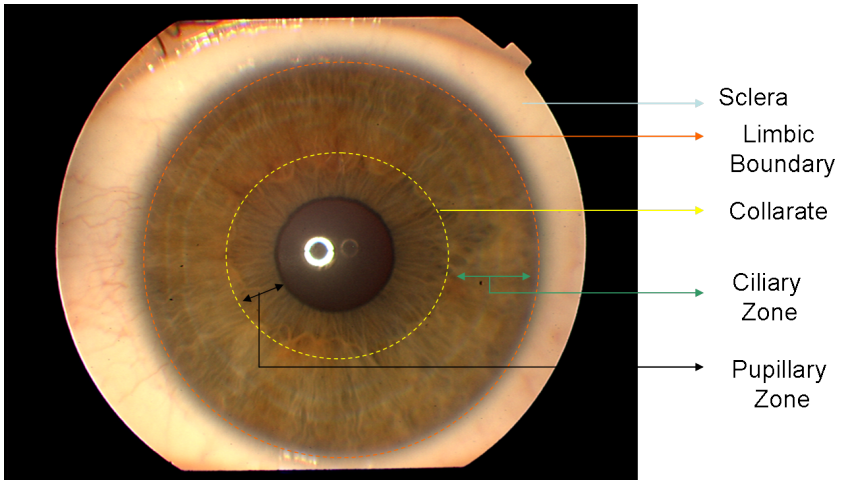

Figure 1.2: Sectional anatomy of the iris

of light that enters the eye by controlling the size of the pupil. The iris begins to form during the third month of the gestation period and the distinctive patterns of the iris are completed by the eighth month. The pigmentation of the iris which determines the eye color continues up to the first year after birth. These distinctive texture patterns formed during the gestation period are *assumed* to be stable throughout the lifespan of an individual [9] and is the result of the initial conditions in the embryonic mesoderm and ectoderm from which it develops [10]. Examples of distinctive features of the iris which *may* be considered stable thoughout the lifespan of an individual and result in an iris structure which is random and unique are usually the pigment frill, collarate, radial furrows, contraction furrows, arching ligaments, and Fuch's crypts. The figure 1.3 shows the iris structures.

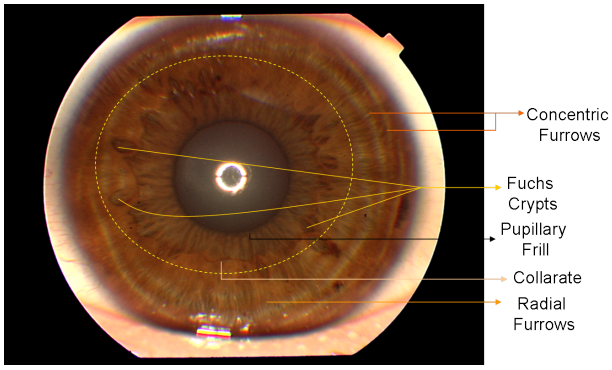

Figure 1.3: Stuctures of the iris

Some other patterns visible in the iris are due to pigmentation. Some examples of pigmentation are due to nevi, tumors or melanoma in the eye, Lisch nodules, Wolfflin Spots, Brushfield spots, Yellow coloration, Central heterochromia, Sectoral heterochromia, and Bilateral heterochromia [2]. Melanomas or tumors are uncontrolled reproduction of melanocytic pigment granules and melanomas in the eye can be intraocular or extraocular. Intraocular melanoma is the melanoma in the uveal tract comprising of the iris, ciliary body, and choroid [11]. Melanoma in the iris is the most uncommon location of primary uveal melanoma, with choroid and ciliary body as common locations in descending order [12, 13]. Iris melanomas are either benign or malignant. Uveal melanomas are mostly diagnosed in older ages [14, 15] and usually occur in caucasians, light color irides, and fair skinned color [11]. Average age of patients diagnosed with iris melanomas is 40 compared to the average age of patients diagnosed with choroidal and ciliary melanoma

which is 50 [13]. Iris melanomas have two patterns of growth: circumscribed and diffused. Circumscribed melanomas usually have flat or rounded anterior contours, whereas diffuse melanomas are present as a unilateral dark iris leading to heterochromia and do not have focal thickening [13]. The iris melanomas are considered to be small, slow growing and dormant compared to other uveal melanomas, and they do not metastasize [16]. They are usually yellow, tan, and brown in color. Some iris melanomas which are clinically less detectable resemble a tapioca. Freckles and nevi in the iris are benign tumors and are usually circumscribed. On the contrary, melanomas are cancerous and usually replace or distort the iris stroma and pupil [15]. Cataract surgeries can change iris texture and require re-enrollment of iris biometric for recognition [17]. Lisch nodules are benign tumors. These are oval or round shaped tumors which are well circumscribed and project from the surface of the iris. Wolfflin and Brushfield spots are white spots around the periphery of the iris. Wolfflin spots are due to clumps of connective tissues and Brushfield spots are due to Down's Syndrome. Wolfflin spots are more distinct compared to the Brushfield spots. Pigmentation such as Central heterochromia, Sectoral heterochromia, and Bilateral heterochromia are due to diffusive growth of iris melanomas. They result in pigmentation of the eye around the pupil (Central Heterochromia), a sector of the iris (Sectoral Heterochromia), and the whole iris in the case of Bilateral heterochromia. In the case of Bilateral heterochromia both the irises of an individual are of different colors. In a study by Wistrand.et.al [18] it is observed that the iridial pigmentation also changes with time during the treatment using latanoprost. The latanoprost treatment results in change in iris color but *may* not cause changes or growth in nevi or melanoma. Figure 1.4 shows examples of the pigmentation features discussed.

1.2 Iris as a Biomarker and Biometric

Iris has been used for two different studies related to psychology and security. Following is a brief discussion on these perspectives of iris where iris characteristics are used as a "biomarker" and as a "biometric".

(a) Lisch Nodules

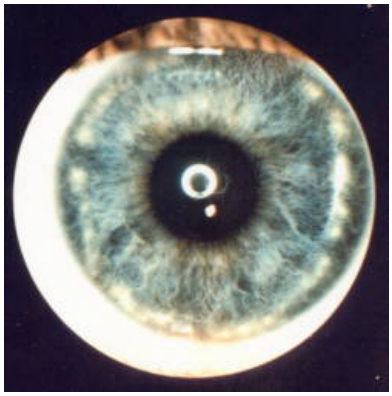

(b) Wolfflin Spots

(c) Bilateral Heterochromia

(d) Sectoral Heterochromia

(e) Central Heterochromia

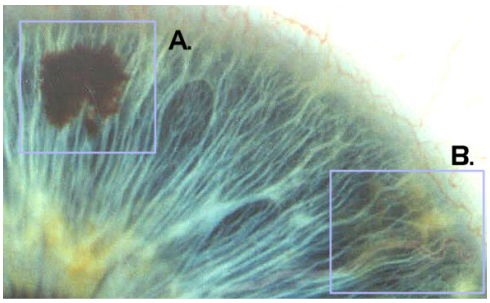

(f) Nevi and Yellow Coloration

Figure 1.4: Examples of pigmentation features. In 1.4(f) block A: example of nevi, block B: example of yellow coloration [2] [3]

1.2.1 Iris as a Biomarker for Personality

In the dissertation by Mats Larsson [19] based on three studies on iris textural characteristics, he concludes that an iris can be used as a biomarker to define an adults personality. Iris characteristics, namely frequency of Fuch's crypts, frequency of pigment dots, iris color, the extension and distinction of Wolfflin nodules, and contraction furrows, were used for this purpose. His studies are based on the heritability of these characteristics [20], the correlation among genes responsible for these iris textural characteristics [4], and the association of iris textural characteristics with the personality of an adult [21].

The experiments were performed on monozygotic twins, dizygotic twins and randomly paired people. Monozygotic refers to like-sex identical twins with most of their genes being shared and dizygotic refers to unidentical twins (includes both like and unlike sex twins) who on average share half of the segregating genes between them. Larsson constructed continuous scales for each of the iris characteristics. Except for iris color, all other characteristics had five continuous scale steps. The iris color has four, namely blue, green, hazel and brown. Figure 1.5 shows examples of the scales used in the experiments [19]. The experiments required, two raters to grade the test images for iris characteristics, according to the scales constructed. Once the grading was completed, the data was analyzed using certain models. The details of the computations are provided in [20, 4, 21].

From each of his studies he concluded that,

a Some of the iris features had higher heritability or higher genetic influences

b There is some degree of correlation between the genes responsible for the various iris characteristics (the correlation measured the extent to which the same genes influenced two iris characteristics)

c The iris may be used as a biomarker for personality in adults.

His first study showed that among the iris characteristics aforementioned, the highest heritability factor was observed for Wolfflin nodules or white dot rings among the older cohort and followed by contractional furrows and Fuch's crypts. The heritability factor is 90, 78 and 66 percent for each of the characteristics. The second study by the author concluded that genetic correlations were not high between some iris characteristics if they had different timings for formation, and if they originated from different processes. For

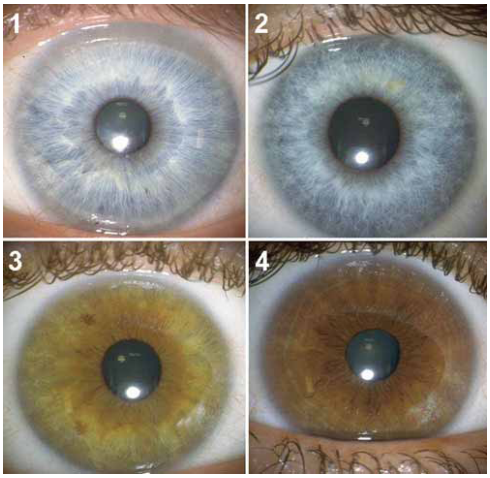

(a) Color Scale

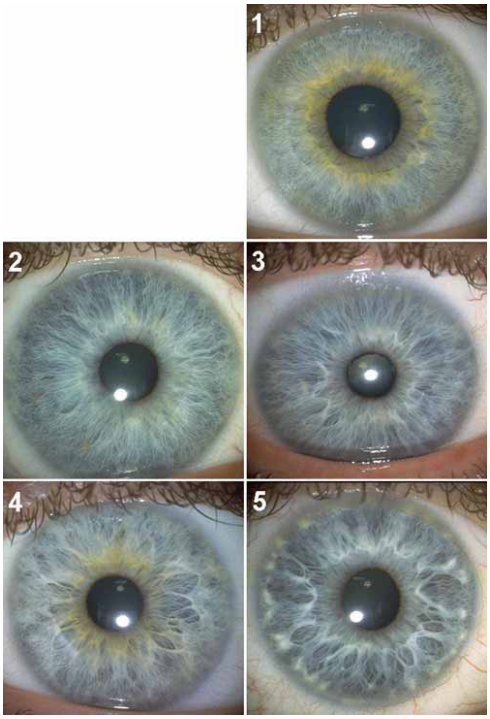

(b) Scale for frequency of Fuch's crypts.

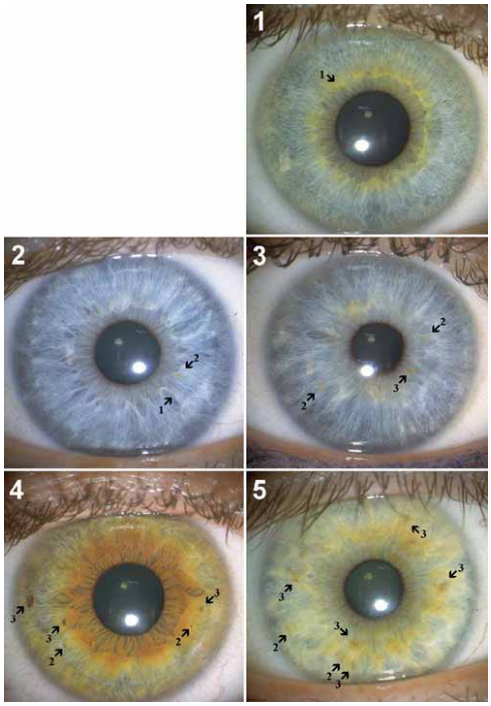

(c) Scale for frequency of pigment dots.

Figure 1.5: The scale constructed by Mats Larsson for iris characteristics, namely color, frequency of Fuch's crypts and frequency of pigment dots [4].

example, the fuch's crypts are present from birth where as the pigment dots start to appear mostly from age 6. On the same lines, the iris color is not determined until early childhood. On the other hand, the Wolfflin nodules are accumulations of fibrous tissue which is different from pigment dots due to melanosomes. The genes responsible for this pair of iris characteristics have insignificant correlation.

In his second study he also observed that the iris characteristics originating from the same cell layers had genetic correlations. For example the contraction furrows which allow the iris to fold with the change in pupil dimensions to allow light, exist in all the layers of the iris. Consequently the contraction furrows have genetic correlation with iris color, Fuch's crypts, and pigment dots in decreasing magnitude.

From the above two studies, it is observed that the iris characteristics are due to certain genes and that they have a certain degree of correlation among them. It would be possible to have these characteristics as biomarkers to adult personality if the genes responsible for these characteristics are also responsible for personality traits. The left hemisphere of the brain is responsible for approach related behaviors and studies show that the genes which may directly influence the formation of crypts and contraction furrows, that is degeneration of the anterior layer of the iris, do cause tissue loss in the left hemisphere of the brain. This may help determine the extent by which people engage in approach related behaviors by observing the iris characteristics. Apart from Fuch's crypts and contraction furrows, pigment dots may influence personality though there is not much evidence. The author showed that the frequency of crypts is related to approach related behavior and that more number of personality traits are associated with crypts. From his studies he also showed that crypts with dense structure score more on traits than crypts with open structure. That is, dense crypts are related to lesser tissue loss in the left hemisphere of brain and score more on approach related behaviors such as openness,warmth, and positive feelings. Also, from the analysis it was observed that the pigment dots are not associated with any of the dominant personality traits. Finally, in his third study, concluded that the iris characteristics could be used as biomarkers for personality. It is not in the scope of this thesis to describe the analysis methods used.

1.2.2 Iris as a Biometric

In another field of study, "Biometric Recognition", the iris has been used to identify a person or to verify the identity claimed by a person. Biometrics measure the physical or behavioral attributes of a person statistically analyses the data. A biometric system is an automated or semi-automated system which makes use of the measured attributes in order to establish the identity of a person. The physical and behavioral attributes used in the field of biometrics are fingerprints, face, iris, hand geometry, gait, and keystrokes. A biometric attribute must possess certain properties to be considered ideal for a biometric system. The properties are:

A. Universality : Everyone in the population must posses the biometric attribute.

B. Uniqueness : The attribute should be unique for each individual.

C. Permanence : The biometric attribute must not change over a period of time. That is with passage of time the attribute must remain stable.

D. Collectability : The attribute should be easily procured from an individual without being invasive.

E. Acceptability : The attribute should be such that the population is willing to provide it. Due to some inhibitions and cultural values the population may not be willing to provide the biometric.

In a biometric system an identity can be established in one of two ways, "identification" or "verification". Identification is the process in which the question 'Who is this person?' is answered. That is, the system tries to identify a person based on the biometric data. Verification is the process in which the question 'Is the person who he claims to be?' is answered. This process verifies the identity claimed by comparing the biometric data of the user and the claimed identity. The above system can be summarized as a biometric recognition system operating either in the "identification" mode or "verification" mode. In this thesis we focus on the iris as a biometric trait. The following is a brief discussion on an iris based biometric.

Iris Recognition System

The randomness in the texture content formed during the initial conditions of the embryonic mesoderm has made it possible to use the iris as a biometric for the purpose of recognition (identification, verification). Figure 1.6 shows the steps involved in an iris recognition system. In a recognition system features of the query image whose identity is to be established is compared either with all the images in the database under "identification" mode or the features of the claimed identity under "verification" mode.

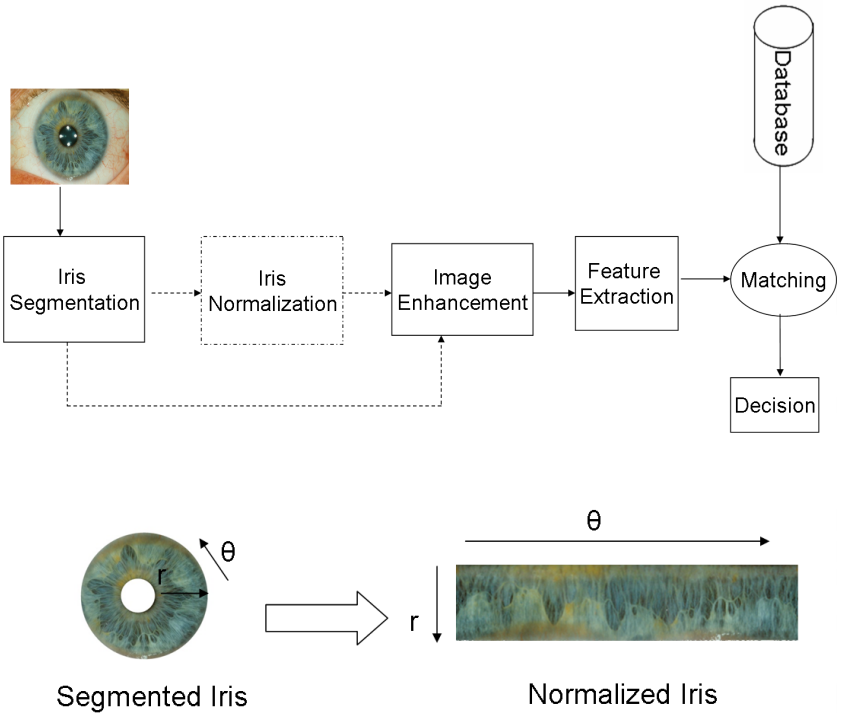

Figure 1.6: Iris Recognition System

Segmentation, normalization, image enhancement, features extraction and matching are the key steps involved in an iris-recognition system. Segmentation is the process in which an iris is segmented from the captured image of the eye. The captured image may be a grayscale or a colored image. Many image processing methods may be applied to obtain a segmented iris image. Segmentation of the iris requires localization of two boundaries namely, iris-pupil boundary and the iris-sclera boundary. Some of the techniques

used for the purpose of segmentation are: Daugman's Integro Differential operator, Libor Masek's Hough transform, and Geodesic Active Contours [22, 23]. Once the boundaries are localized, it is assumed that the pupil and iris are circular. The pupil and iris are segmented by fitting circles with radius equivalent to the radius of the pupil and iris. The iris is then finally represented as a circular disc.

The next step is optional. It is usually based on the way the features are extracted from the image for the purpose of recognition. This step is normalization or unwrapping, where the circular iris is transformed from a circular entity in the Cartesian coordinate system to a rectangular entity in the polar coordinate system. This transformation is done using Daugman's rubber sheet model [24], which transforms the points within the iris to polar coordinates (r, θ), where r lies between 0 and 1 and θ lies between 0 and 2π. The r represents the radial distance from the iris-pupil boundary to iris-sclera boundary, and θ represents the angle subtended by a pixel relative to horizontal axis at the origin, with the origin at approximately the center of the pupil. The following is the equation used for the transformation:

$$I(x(r,\theta), y(r,\theta)) \rightarrow I(r,\theta)$$

Here $x(r,\theta)$ and $y(r,\theta)$ are pixel positions within the circular disk and defined as a linear combination between points on the pupillary boundary, $(x_p(\theta), y_p(\theta))$ and the iris-sclera boundary, $(x_s(\theta), y_s(\theta))$. The points within the iris are defined as,

$$x(r,\theta) = (1-r)x_p(\theta) + rx_s(\theta)$$

$$y(r,\theta) = (1-r)y_p(\theta) + ry_s(\theta)$$

The normalization procedure helps to transform every iris to a predefined size. This avoids the scaling issues due to pupil dilations and different diameters of the iris. The image is then enhanced to perform photometric normalization. Here all the irises are enhanced to have the similar luminosity and contrast. The simplest technique for contrast enhancement is the histogram equalization.

The features are then extracted, either from the normalized iris or the circular iris. The literature discusses many techniques to represent the iris in order to perform recogni-

tion. These techniques can broadly be classified into four categories, namely Phase based methods, zero crossing representation, texture analysis and intensity variation analysis.

Flom and Safir [9] had proposed the concept of automated iris recognition. In 1994 John Daugman had patented his "Biometric Personal Identification System Based on Iris Analysis". Daugman used multiscale Gabor filters to demodulate texture phase structure information of the iris. This information was binarized and used for recognition using hamming distance as the distance metric. Wildes [25] represented the iris texture with a Laplacian pyramid. Boles and Boashash [26] characterized the iris texture by calculating zero-crossing representation of the one-dimensional wavelet transform at various resolution levels of a concentric circle on an iris image. Park et al. extracted the normalized directional energy as features and Bae et al. [27] used the quantized results of the projection of iris signals on filter banks derived by independent component analysis as features. In each of the techniques the iris texture which is a result of characteristics such as crypts, furrows, pigment dots, arching ligaments has been encoded [28]. The whole of the iris texture is encoded without discrimination of each of the characteristics responsible for the iris texture.

There have been attempts to extract and characterize the micro features of the iris in the past. Micro features in this thesis, refer to any textural features that have not traditionally been focussed upon. Sung et al. [29] proposed to localize the collarate boundary and perform iris recognition using only the collarate region as the textural feature. Also, Wen et al. [30] obtained the key locations that is the barycenter of iris features extracted by Gabor filtering, and computed the Euclidean distance between barycenters of two images to measure the similarity. Although the features extracted are digital features due to intensity variation in each of the filtered sub-images, they may not in particular represent the macro features such as the freckles, nevi, or blood vessel patterns. Another attempt was to extract four micro features, namely the nucleus, collarate, valleys and radius and consider them as minutiae for identification. Nucleus are the possible zones inside the contour of the pupil which do not satisfy circular symmetry. Collarate is the zig-zag pattern which divides the iris into the pupillary zone and the ciliary zone. It is considered to be the thickest part of the iris. Valleys correspond to zones of intense pigmentation of the iris in the pupillary zone. The radius feature corresponds to the intensity variation to-

wards white color compared to the intensity of the iris. The matching counts the number of corresponding micro features [31]. Figure 1.7(a)1.7(b) show the features considered by proposed techniques of Sung et al. and Wen et al. [29, 30].

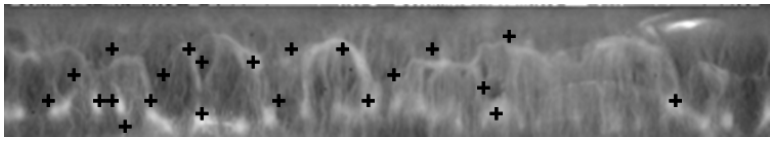

(a) Keypoints used for iris recognition [30]

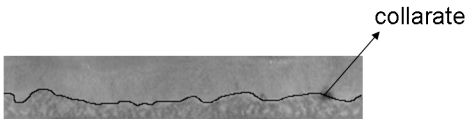

(b) Collarate region used for recognition [29]

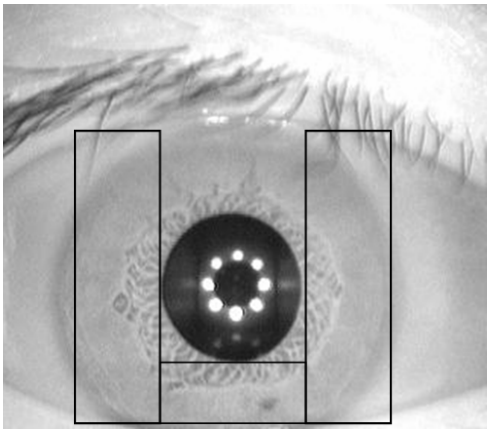

(c) Iris regions used by the SIFT technique [32]

Figure 1.7: Examples of non-traditional iris features used for recognition

Each of the above techniques used a normalized iris. In a recent paper by Belcher and Du [32], they performed iris recognition using SIFT points detected by matching the relative orientation and magnitude of the gradient and the relative position of each point within a window W with respect to the feature points detected. This approach did

not require iris normalization. The feature points detected are extrema points, that is they are the maximum or minimum intensity points. This is a region based approach in the sense that feature points are detected in different regions of the iris, namely the left, right, and bottom portion of the circular iris around the pupil. Figure 1.7(c) shows the iris regions considered for feature point detection. The feature points detected in each of these regions is matched to the feature points of the corresponding region. This approach is extended by the authors for iris recognition of off-angled irises where the iris is not at the center of the eye.

Matching is the process of comparing the features of a test image with the features of images in the database. As mentioned earlier, in a verification based system a test image's feature set is matched against those of claimed identities stored features in the database. This is a one-to-one matching. In an identification-based system, the features of the test image are matched with all the stored features in the database in order to find the closest match from the database, which in turn would decide the identity associated with the test image. This is a one-to-many matching. Each match results in a match score. The matching metric used depends on the type of features extracted. For instance, in Daugman's iris recognition system, matching is performed using the Hamming distance while in the SIFT based method [32] the Euclidean distance is used to match the features.

1.3 Motivation

As explained above, an identification-based system requires one to many matching. The current iris recognition systems are fast and perform a large number of one-to-one comparisons in a second. The iris recognition system deployed in Dubai performs around 420,000 comparisons per second [33]. But with the growing size of the database the number of comparisons increases, increasing the computational complexity. Thus, there is need to reduce the search space for recognition systems. That is, the number of identities a query image is compared against has to be reduced. The two ways by which the search space can be reduced are classification and indexing. Classification of images in a database involves partitioning the database into subsets based on certain characteristics. These subsets may not be mutually exclusive. The search space for a query image will be

limited to the subset it is classified to. For example, fingerprints are typically classified into 5 classes. They are based on the type of ridge flow observed on the print. The classes are whorl, left loop, right loop, arch, and tented arch. The classification results in subsets which are not of uniform size. Further, these subsets are small in number [34]. The classification process still results in a large subset of candidate identities. Indexing, on the otherhand, reduces the search space significantly. Indexing works by assigning a numerical value to the biometric data based on the features or match score. Once the query image is assigned an index value, it is compared with the set of stored images which have similar index values. This reduces the search space to the top m identities with similar index values. The importance of reducing the search space for faster and reduced number of comparisons is clearly seen.

The increasing computational complexity with increasing datasize has motivated us to focus on textural features which can be used for grouping of iris texture. Some of the other characteristics we propose to detect may also establish a new set of features for the purpose of recognition of two iris images. These new features may represent the new set of minutiae points within the iris which may be used for matching two iris images. A Match between the iris images is established by determining the number of minutiae correspondences. These features may also be used for the purpose of indexing based on their location and characteristics on an iris image. Chapter 2 discusses the features extracted and the experimental setup for the purpose of classification. Chapter 3 discusses the different approaches for the detection of macro features proposed by us such as, pigment dots, nevi, and freckles. These characteristics may be used for iris recognition and image retrieval.

Chapter 2

Iris Texture Classification

2.1 Introduction

As mentioned in chapter 1, due to the chaomorphogenic nature of formation of iris, it is one of the most reliable biometric for the purpose of recognition. No two irises, even the left and the right iris of an individual are expected to be identical. A typical biometric recognition system operating in identification mode requires that features extracted from a query image be compared with features of the enrolled identities in the database to determine the identity. The identity is determined when the result of matching satisfies a criteria for establishing the identity. Matching is the process of comparing the features extracted from the query image with features extracted from images in the database. Figure 2.1 shows the modules of a biometric recognition system.

In the case of iris biometric recognition system, typically a query iris image is subjected to segmentation, normalization, may be enhancement before feature extraction, and matching. As mentioned in Chapter 1, fingerprints could be classified to 5 classes at a preliminary level based on the orientation of the ridges. In the case of iris there is no such coarse level classification. As mentioned earlier, in the case of "identification", a number of one-to-one matches are performed. Though iris recognition systems can perform a large number of one-to-one comparisons efficiently and with high accuracy, with the increasing size of database the computational processing increases. For example, the most efficient deployment of an iris recognition system performs iris recognition for a

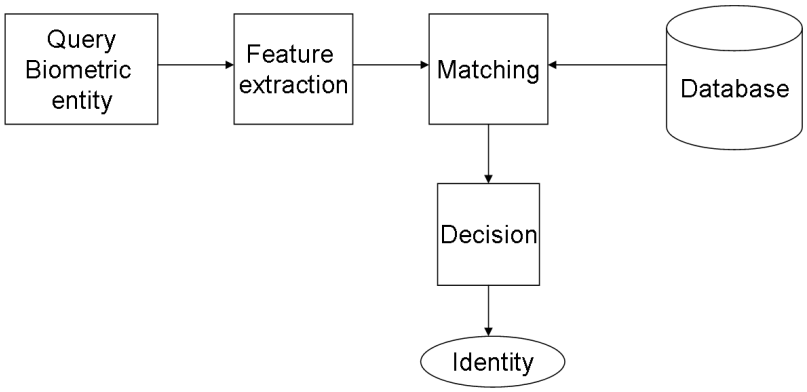

Figure 2.1: A biometric recognition system operating in identification mode

query image using multiple servers [33].

The search space which is the number of identities to which the query image is compared can be reduced by two techniques, classification and indexing. Classification is the process in which the database is clustered to a pre-determined set of classes based on the features extracted. A query image is then assigned to one or more of these classes and is compared with all the identities present in the class to determine the identity. Indexing involves retrieval of top m identities based on comparison of the index values assigned to each entry in the database. The index values can be a vector entity **??** and are compared using a metric to retrieve the top m closest matches. These m identities are then exhaustively compared with the query image. Figure 2.2 shows a recognition system in which the identification is performed using the classification technique in which the database is partitioned into a number of classes.

Classification and indexing are the algorithmic solutions for faster matching results by reducing the search space. Some indexing techniques are discussed in [34, 35]. Though the iris texture is due to the chaomorphogenic nature, the focus of this thesis is to determine if the irises can be partitioned to groups based on similarity in the textural content.

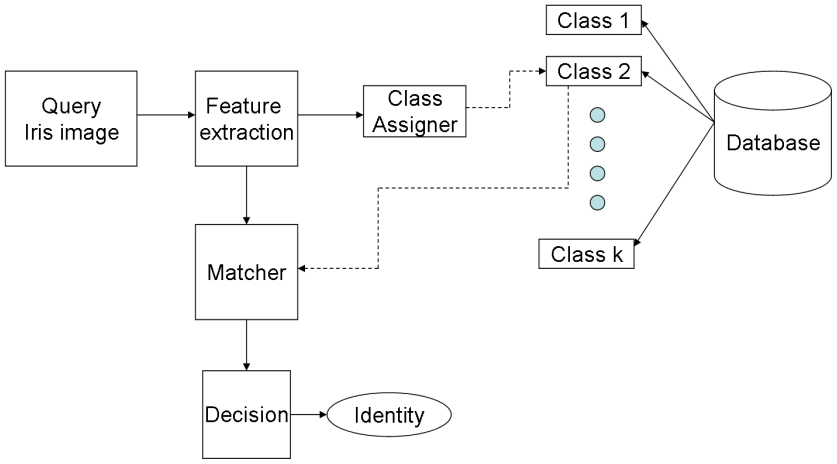

Figure 2.2: An identification system using classification technique

2.2 Literature survey on iris classification based on texture

As mentioned in Chapter 1, the iris is composed of many layers and many components such as arching ligaments, Fuch's crypts, contraction furrows, radial furrows, collarate and other pigmentation structures. The iris texture is considered to be stochastic, as it is random due to the presence of many iris characteristics and depends on the initial morphogenesis in the mesoderm. Most applications involving iris such as iris recognition, iris classification and iris indexing are performed by analyzing its texture using texture analysis methods. Figure 2.3 shows examples of irides with different textures.

Fingerprints can be classified to 5 classes at a preliminary level based on the orientation of the ridges. In the case of iris there is no such coarse level classification of iris except for the manual scales described by Mats Larsson in [19]. An automated iris classification based on the difference in texture due to the presence of Fuch's crypts is discussed in [5].

Iris texture has been analysed, both for the purpose of classification and indexing. Some examples of iris classification and indexing using textural features are discussed in [34, 6, 5]. An iris classification system would require image preprocessing (segmentation of iris, normalization, enhancement), and feature extraction using texture analysis methods. Figure 2.4 depicts the flow of a classification algorithm for iris.

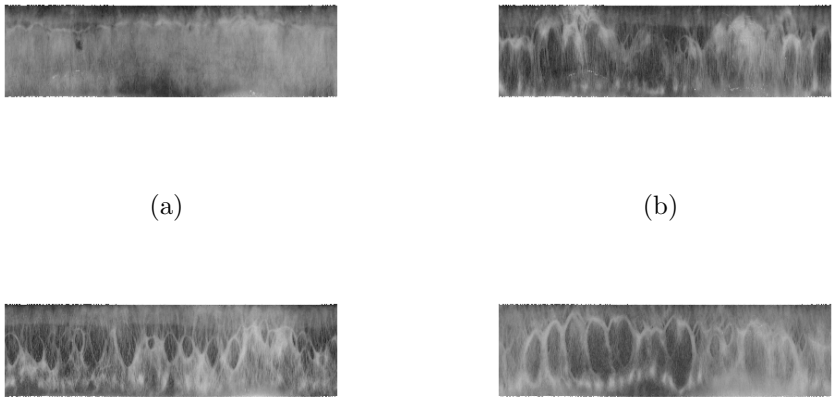

(a) (b)

(c) (d)

Figure 2.3: Examples of iris textures

Two examples of classification based on iris texture analysis are: classification of iris texture to pre-determined number of classes [5] and classification of ethnicity based on iris texture analysis [6]. The latter assigns the iris only to two classes namely, asian and non-asian.

According to [5] the iris is classified to pre-determined number of classes namely, net structure, silky structure, linen structure and hessian structure. Texture analysis is performed only on the circular iris disk corresponding to $\frac{3}{4}$ of the iris radius. The $\frac{3}{4}$ iris is considered to avoid occlusions due to eyelashes and eyelids. This portion of the iris is first normalized to 64 x 256 and the texture analysis is performed by computing the fractal dimension [36] of 32 x 32 blocks from the middle and lower part of the normalized iris. This results in 8 block each from the middle and the lower part of the normalized iris. Figure 2.5 shows the portion of the normalized iris considered for texture analysis, and the blocks considered for feature extraction. The classification accuracy is evaluated by counting the number of times the sample queries of the same subject are assigned the same class as that of the enrolled identity of the same subject.

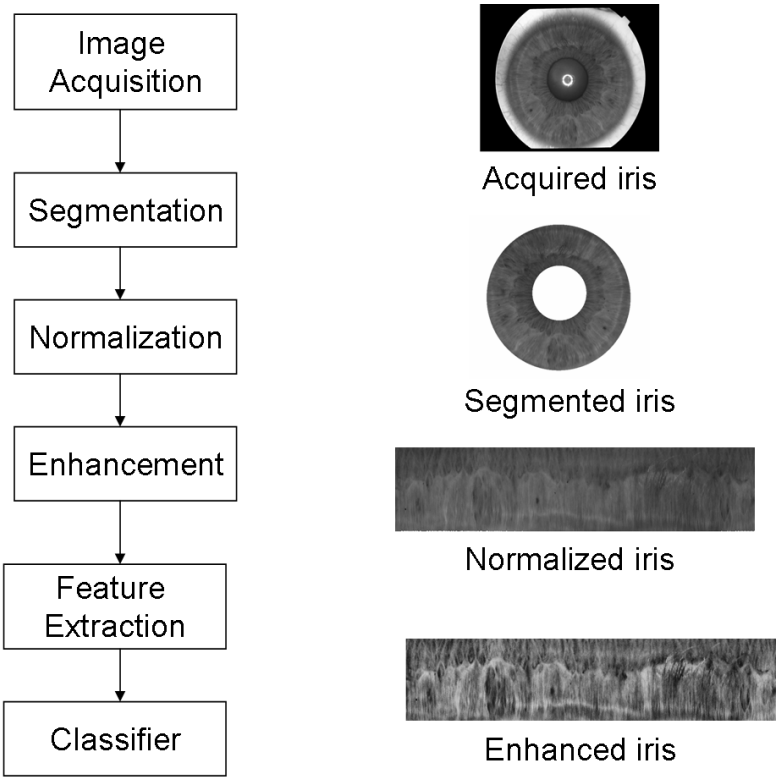

Figure 2.4: Iris texture classifier

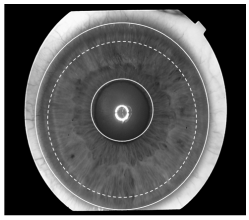

(a)

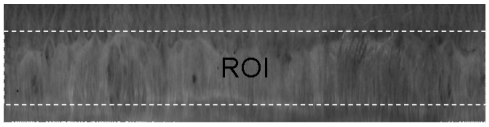

(b)

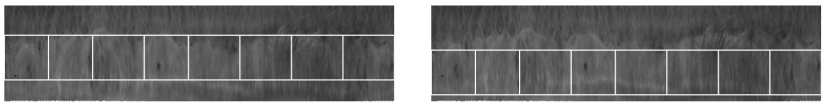

(c)

Figure 2.5: (a) ROI is $\frac{3}{4}$ of the iris, (b) normalized ROI, (c) 16, 32 x 32 Blocks of iris for fractal analysis based on [5]

In the ethnicity classification method, the iris texture is analyzed to classify the query image's ethnicity as Asian or Non-Asian [6]. The work tries to relate texture to ethnicity. The iris texture at a coarse level is analyzed assuming that the iris texture is correlated to genes at large scale. Like in the previous iris classification technique, the iris texture considered for analysis is the inner $\frac{3}{4}$ of the lower half of the segmented iris. The iris image is enhanced and normalized such that the region of interest is 60 x 256. This region of interest is equally divided to two regions: region A and region B, as shown in figure 2.6.

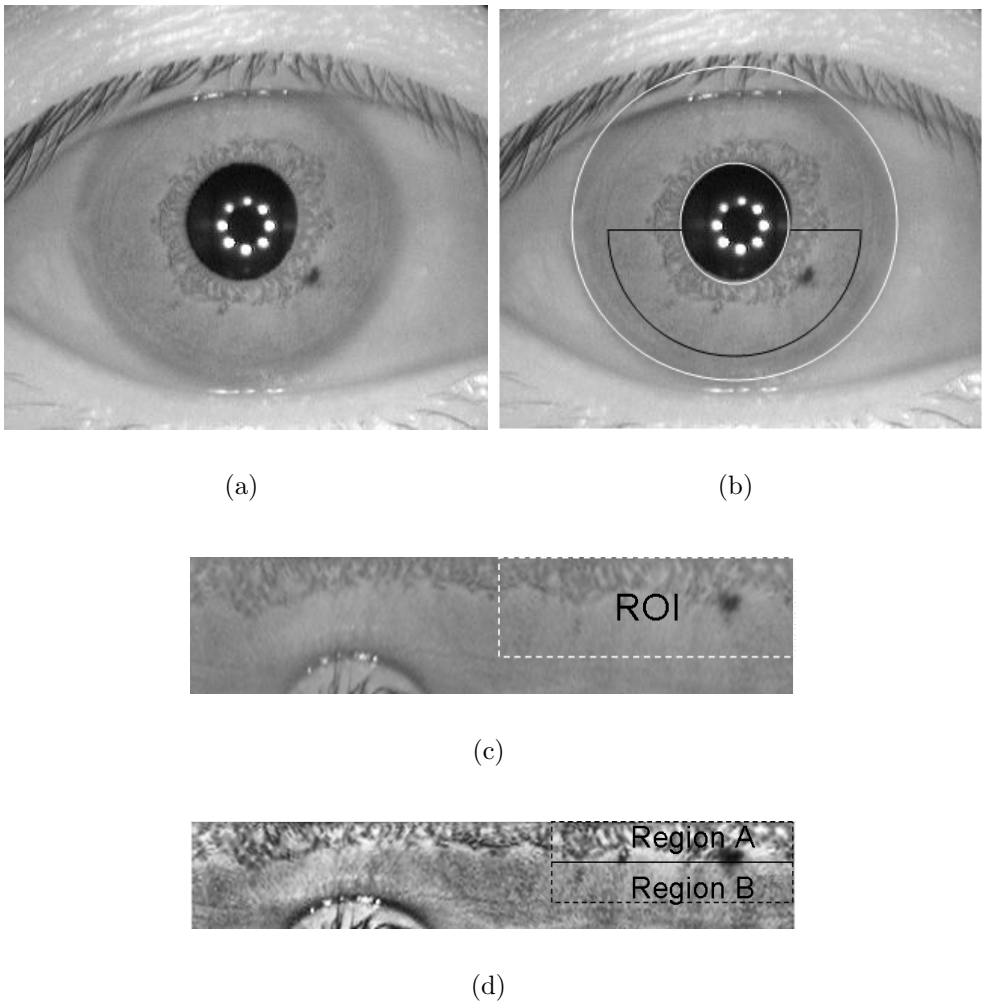

(a) (b)

(c)

(d)

Figure 2.6: Extraction of ROI. (a) Acquired image, (b) Iris localization and ROI, (c) Iris normalization and ROI, (d) ROI after enhancement. Images based on [6]

These regions are filtered using a bank of Gabor filters with 4 orientations (0, 45,

90, 135 degrees), 6 spatial frequencies and 10 space constants [6], resulting in 240 filters. The energy of each of the filter responses is computed using the L2 norm at each pixel location. The Gabor energy(GE, m_b) and Gabor energy ratio(GER, $\frac{m_A}{m_B}$) are extracted from the average energies m_A, m_B of the regions A and B.

In both of these methods the iris texture is characterized using texture analysis. The following sections discuss texture and texture analysis in order to understand the methods which can be used for iris feature extraction.

2.3 Texture

Texture, in general, may be defined as the appearance of an object on a digital image. An image texture is considered to have certain properties [34, 37, 38]:

- A texture is attributed to a set of pixels in the local neighborhood and not to a pixel by itself.
- The gray levels in an image help the human eye visualize texture of an object. Hence, the statistical measures which quantify the gray scale distribution can be considered as one of the tools to measure texture.
- The texture can be measured in terms of coarseness, smoothness, regularity, homogeneity, direction, contrast, density and other statistical measures. These measure the textural properties of an image or regions defined by sets of pixels in an image.

Texture analysis helps in characterizing the texture of an image and extract quantitative textural attributes associated with the texture. The level of features extracted partly depend on the resolution of an image [34, 37]. At low resolution global texture features are captured and at high resolution local texture features are used.

An image may be considered as an agglomeration of a number of visual textures. These visual textures can be either structural or stochastic [39]. By structural texture we mean textures which have repetitive patterns of small elements arranged via some placement rules. Such textures are generated using deterministic or structural methods.

On the other hand there are textures which do not have noticeable elements arranged in a regular pattern. They have random orientation and placements and exhibit random arrangement of different elements of texture. Such textures are generated from stochastic processes.

The textural features which can be extracted are based on statistical, geometrical, model and signal processing based methods [40]. Following is a brief description on the way texture can be analysed.

2.4 Methods of Texture Analysis

2.4.1 Statistical Methods

Statistical methods typically measure the spatial distribution of gray scale values. They measure the statistical relation between pixels in the image [37]. The statistical features measured are typically of second and higher order statistics.

Gray Level Co-Occurence Matrix

The first order gray level histogram represents the probability of occurrence of gray levels in an image [41]. A gray level co-occurrence matrix is considered to measure the second order histogram as it considers gray level distributions of pairs of pixels in each direction [41]. The gray level co-occurrence matrix is defined as $H(x, y, d, \theta)$, where H represents the matrix computing the frequency of occurrence of all pairs of gray level values ((i, j), with i and j in [0, 255], separated by a distance 'd' (dx,dy) in direction 'θ'. That is, in a co-occurence matrix the element (i,j) represents the number of pixel pairs in the image separated by a distance 'd' in a direction θ such that the intensity of the first pixel is "i" and that of the second pixel is "j". There is no criteria to select the distance 'd'. This results in a number of sparse co-occurrence matrices for different combinations of 'd' and'θ'. These matrices do provide some amount of information on the spatial distribution of gray levels with respect to the displacement 'd' and direction 'θ' [40]. For example if the diagonal of a co-occurrence matrix with displacement 'd' is concentrated then the texture is coarse in direction θ. But these matrices are not used directly to analyze texture. Many

Haralick textural features [42] can be computed from these matrices. Some of them are characteristics of texture such as homogeneity(smoothness), contrast, entropy and energy. These features can be used in isolation, or combinations of these features can be used for classification. Following are the formulas used to compute certain textural features from the co-occurrence matrix M(i,j) where, μ_x, μ_y and σ_x and σ_y are the means and standard deviations of M(x) and M(y) where, $M(x) = \sum_j M(x,j)$, $M(y) = \sum_i M(i,y)$.

i Energy - $\sum_i \sum_j M^2(i,j)$

ii Entropy - $\sum_i \sum_j M(i,j) \log M(i,j)$

iii Contrast - $\sum_i \sum_j (i-j)^2 M(i,j)$

iv Homogeneity - $\sum_i \sum_j \frac{M(i,j)}{1+|i-j|}$

v Correlation - $\frac{\sum_i \sum_j (i-\mu_x)(j-\mu_y)M(i,j)}{\sigma_x \sigma_y}$

Auto-correlation

Texture is considered as a repetitive placement of a textural pattern or "texton". This measure quantifies the property of repetitive placement of patterns in a textured image. It measures the regularity, fineness or coarseness of the texture in an image. The auto-correlation of an image I(x,y), is defined as,

$$\rho(x,y) = \frac{\sum_{u=0}^{N} \sum_{v=0}^{N} I(u,v) I(u+x, v+y)}{\sum_{u=0}^{N} \sum_{v=0}^{N} I^2(u,v)}$$

It measures the correlation between the pixel and its surrounding pixels in an image or correlation with a subimage. The autocorrelation function depends on the size of texton. The texture can be known from the response of an autocorrelation function. For example for coarse textures the autocorrelation function drops of slowly where as for fine textures it drops off sharply. For textures exhibiting regular patterns in the image the autocorrelation function is periodic with peaks and valleys.

2.4.2 Geometrical Methods

Geometrical methods are used to analyze textures which are regular patterned or composed of texture elements or primitives. In other words these methods analyze tex-

tures which are repetitive or textures formed due to arrangement of texture primitives. Geometrical methods are used to measure the geometric properties of the primitives or texture. The geometric methods extract the placement rules describing the texture of an image. Following is a brief discussion on one example of the geometric method for texture analysis.

Structural Methods

This method of analysis is used for textures which have repetitive patterns which are placed according to some placement rules. The efficiency of the algorithm is limited to regular structures. The texture analysis consists of extraction of texture primitives and inference of placement rules for these texture primitives. The texture elements are considered as regions with uniform gray levels. Multi-scale analysis and blob detection techniques are used to extract the texture elements. Some additional features such as shape and intensity are extracted from detected elements. In another work the placement rule is defined as a tree grammar [40, 43]. This method can be used both for texture generation and texture analysis [40].

2.4.3 Model Based Methods

This method also constructs a texture model which not only describes the texture but can also be used for synthesizing the texture. The goal of the model is that the parameters capture the perceived qualities of texture. Markov Random Fields are widely used for modeling the images. The textural model is based on the statistical interactions within the local neighborhoods. That is, an intensity of a pixel depends to a large extent on the neighboring pixel intensity. Markov fields capture the spatial contextual information in an image. It has been used in many image processing applications such as image segmentation, image compression and restoration. It is also applied for texture synthesis and texture classification.

Fractals is another model used in this method of analysis. It is based on the fact that most images conform to the statistical property of texture "roughness" and that they have self similarity at different scales. Self similarity in a image refers to the multiple scales of a texture primitive arranged randomly. Fractal dimension is the measure of

texture using fractals. For a deterministic texture the higher the value of fractal dimension the rougher is the texture. But most textures are not deterministic. They have certain statistical variation and are categorized as stochastic textures. This makes computation of fractal dimension to model texture difficult. Fractal dimensions fail to capture all textural properties. Lacunarity is the metric to measure texture with same fractal dimensions [44].

2.4.4 Signal Processing Based Methods

In texture analysis using signal processing methods, features are extracted from the filtered responses of an image [40, 37]. Either spatial domain or frequency domain filters can be used. These features can be used for classification or segmentation. Usually the features extracted from the responses of the frequency domain filters perform the best. This is based on research in psychophysics that humans perform frequency analysis on texture. The human brain analyzes an image by decomposing it to frequency and orientation components. Along the same line the concept has been extended to decomposing the image to frequency and orientation components by using banks of filters with different frequencies and orientations. This method is also referred as multi-resolution processing. The filtering is performed in Fourier domain and it also obtains phase information which helps in classifying or segmenting images comprising of texture with similar intensity and textural features but varying in phase. For example two images with black and white horizontal bars, one image starting with white bars and the other black bars. These two images can be differentiated using the phase information.

This concept is further extended to the multi scale processing using wavelets and Gabor filters. Here the image is decomposed to a set of frequency and orientation components along with the scale of the image being reduced. Further applications require that there is spatial localization. This is achieved using window filtering or short term Fourier transform. In case of Gabor filters the window is defined by the Gaussian kernel.

2.5 Proposed Technique

To study the iris texture and its ability to be grouped, we propose to extract statistical textual features from iris and group the iris texture based on the textural features. Both

signal based and statistical texture analysis is performed to extract textural features. The proposed technique performs iris classification by classifying block of a query image to one of the pre-determined clusters or classes using the minimum distance rule. The clusters are obtained by partitioning the database using the textural features extracted from a certain block of iris. In order to obtain pre-determined number of clusters, the features extracted from the iris image database are subjected to unsupervised clustering using the principal direction divisive partitioning method (PDDP) [45]. The query image block to be classified is subjected to textural analysis and is assigned the class based on the minimum distance rule. The minimum distance rule is used to compute the distance between the feature vector of the query image and either the cluster centroid or the features corresponding to each sample in the cluster class. Assigning a query image to one of the clusters by comparing its features with the cluster centroids is the centroid based classification scheme and assigning the query image to one of the clusters by comparing the features of the query with the elements of clusters is the K-Nearest Neighbor classification scheme. In K-Nearest Neighbor classification scheme, the query image is assigned to the cluster represented by a majority of the k-closest neighbors. The query iris texture is classified by minimizing the cosine angle between features of the query iris and that of the cluster centroid or elements of a cluster. The cosine distance measures the similarity between two features vectors $\mathbf{f}_1$ and $\mathbf{f}_2$ as,

$$Angle = cos^{-1} \frac{\mathbf{f}_1.\mathbf{f}_2}{\|\mathbf{f}_1\|.\|\mathbf{f}_2\|}$$

The smaller the angle the larger is the similarity between the two features. For the purpose of analysis of the proposed approach, textural features are also extracted from the synthesized iris images. The iris images are synthesized using the textural features extracted from the original iris images in the database resulting in a synthesized iris image for each of the iris images in the original database.

2.6 Feature Extraction

The iris image is pre-processed to obtain the region of interest from the the features are extracted. This is discussed in the following sections.

2.6.1 Region of Interest

The normalized iris is not free from noise such as eyelids, eyelashes, and specular reflections. The pupillary zone, the portion of iris from the pupil-iris boundary to the collarate of iris, is rich in texture and not adversely affected by eyelids and eyelashes. In order to minimize the effect of noise we consider blocks from the inner half of the normalized iris corresponding to pupillary zone for feature extraction. The region of interest (ROI) is the iris region from the iris-pupil boundary upto half of the iris radius. Figure 2.7 shows the outputs of preprocessing steps, region considered for feature extraction (region of interest, ROI), and blocks of iris considered for feature extraction. Overlapping blocks of height = 32 and width = 2^i, where $6 \leq$ i ≤ 9 are considered for feature extraction. The blocks for each width are numbered progressively from the left to the right of the normalized image. For example, blocks of size 32 x 64 are numbered from 1 to n_{reg} from the left to the right of the normalized iris, where n_{reg} is the total number of blocks obtained of size 32 x 64. Similarly regions of different widths are numbered from 1 to the total blocks of width 2^i obtained from the normalized iris, such that $6 \leq i \leq 9$. The features of each of these blocks are extracted, both for original and synthetic iris images using the texture analysis algorithm proposed by [7]. The following section discusses the feature extraction technique adopted for texture analysis.

2.6.2 Feature Extraction

Both model based and signal based texture analysis methods used for the purpose of iris texture classification [5, 6]. Since human brains process visual information by decomposing it to frequency and orientation components [40] and the iris image requires statistical analysis due to the non-deterministic chaomorphogenic nature of texture, texture analysis using both of these methods via statistical analysis on the filtered signals is proposed. The filtered signals are obtained as a result of convolving image with linear kernels oriented at multiple spatial scales. One advantage of characterizing an image with statistical features is that it provides a compact representation of an image and an approximation of the original texture can be synthesized using the features extracted. Features are extracted from different regions of original iris texture as well as the synthesized iris texture. The iris texture is synthesized using the features extracted from the original iris

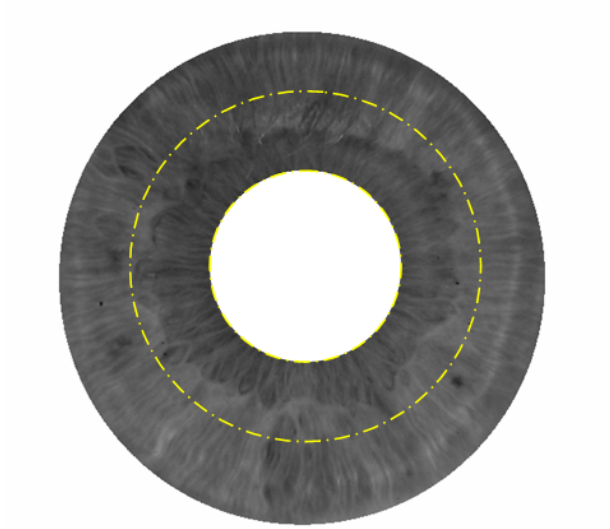

(a) Segmented Iris

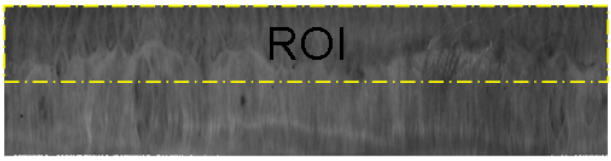

(b) Normalised Iris

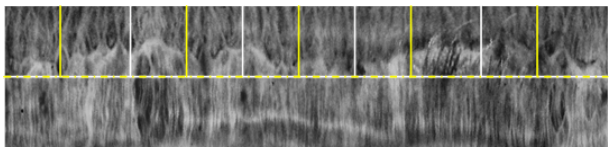

(c) Enhanced Image

Figure 2.7: The output of the preprocessing steps along with the region of interest. The white and yellow boxes in 2.7(c) show the overlapping blocks on the enhanced image considered for feature extraction

texture [7].

Portilla and Simoncelli [7] extract the statistical features from the complex multi-scale wavelet representation of the texture. The complex multi-scale wavelet representation is obtained by decomposing an image using steerable pyramids, which, decompose images at different scales and orientations using complex filters. The statistical textural features are extracted from the iris blocks decomposed using complex steerable pyramid to 2 scales and 4 orientations. The frequency response of the steerable pyramid is implemented by initially decomposing an image to low (L) and high pass residual (H). The low pass residual is then recursively decomposed to orientated band pass (B_k) and low pass residual bands at each scale. The filters used are polar separable in Fourier domain and are represented as:

$$L(r,\theta) = \begin{cases} 2\cos(\frac{\pi}{2}\log_2(\frac{4r}{\pi})), & \frac{\pi}{4} < r < \frac{\pi}{2} \\ 2, & r \leq \frac{\pi}{4} \\ 0, & r \geq \frac{\pi}{2} \end{cases} \tag{2.1}$$

$$B_k(r,\theta) = H(r)G_k(\theta), \qquad k \in [0, K-1], \tag{2.2}$$

where K is the total number of orientations and H(r) and $G_k(\theta)$ are the radial and angular parts written as,

$$H(r) = \begin{cases} \cos(\frac{\pi}{2}\log_2(\frac{2r}{\pi})), & \frac{\pi}{4} < r < \frac{\pi}{2} \\ 1, & r \geq \frac{\pi}{2} \\ 0, & r \leq \frac{\pi}{4} \end{cases} \tag{2.3}$$

$$G(\theta) = \begin{cases} \alpha_K[\cos(\theta - \frac{\pi k}{K}]^{K-1}, & |\theta - \frac{\pi k}{K}| < \frac{\pi}{2} \\ 0, & otherwise, \end{cases} \tag{2.4}$$

r, θ are polar frequency coordinates and $\alpha_K = 2^{k-1}\frac{(K-1)!}{\sqrt{K[2(K-1)]!}}$. Figure 2.8 shows the iris blocks and the and magnitude responses of iris blocks at 2 scales and 4 orientations.

The textural characteristics of the iris image are represented by the pixel intensity distribution, visual description such as coarseness, fineness, and regularity due to periodic or globally oriented features like radial furrows, crypts at different scales, contraction furrows and pigments spots. Apart from this, the crypts and furrows at different scales

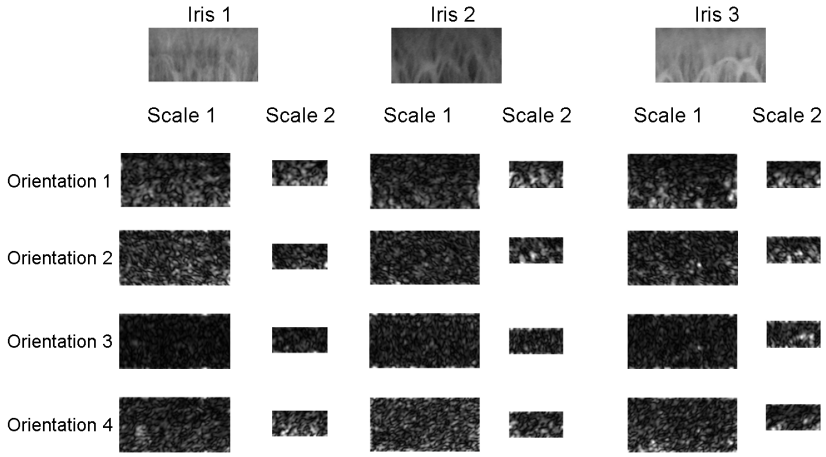

Figure 2.8: Iris blocks and corresponding responses

produce oriented edges and corners. These features representing the iris texture may be captured using first, second, third, fourth order statistics, and correlation features from the original iris image and the decomposed subbands of the iris.

The relative amount of each intensity and the visual description of the iris image is measured from the original image and low pass bands at each scale by computing the minimum, maximum, mean, variance, skewness and kurtosis. The low pass bands are reconstructed at each scale from the real or imaginary parts of the oriented bands. The spectral features which represent periodicity (spectral peaks) and ridges (globally oriented structures) are usually captured by computing the local autocorrelation of the lowpass residuals at each level of the pyramid decomposition. The high contrast regions oriented at each scale such as the edges, bars and corners are captured from the cross correlation statistics. The cross correlation is computed between the magnitudes of each oriented bandpass response at a scale with the magnitudes of the oriented bandpass responses at the same scale and a coarser scale. Given an image I with total number of pixels $|I|$, pixel intensities x_i and mean of all intensities m, the variance skewness and kurtosis are computed as,

$$Variance, \sigma^2 = \frac{1}{|I|} \sum_{1 \leq i \leq |I|} (x_i - m)^2, \tag{2.5}$$

$$Skew = \frac{1}{|I|} \sum_{1 \leq i \leq |I|} \frac{(x_i - m)^3}{\sigma^3}, \tag{2.6}$$

$$Kurtosis = \frac{1}{|I|} \sum_{1 \leq i \leq |I|} \frac{(x_i - m)^4}{\sigma^4}. \tag{2.7}$$

All the statistical features computed are concatenated to form a feature vector F_i of dimension 68 for each of the iris blocks considered.

The above mentioned features are extracted both from the original images and synthesized iris images. Texture synthesis is the process of generating the textured image which has been characterized using the textural features or constraints. Each of the extracted textural features are considered as a constraint for the purpose of synthesis. The textural features are represented as Φ_k with values, c_k, where $1 \leq k \leq N_c$ and N_c is the total number of constraints. Portilla and Simoncelli [7] include some additional constraints for texture synthesis. The criteria of texture synthesis is that the constraints of the synthesized texture be the same as c_k, that is if I_1 is the original iris texture with c_k as the values for the statistical feature set, then the synthesized texture I_2 must satisfy,

$$E(\Phi_k(Y)) = c_k, \qquad \forall k$$

where E is the expected value of the texture parameter measured over the synthesized image.

A synthesized texture I_2, having the same textural measurements as of I_1, is obtained by selecting a high entropy distribution, such white Guassian noise ($\overrightarrow{x}^{(0)}$) with the same mean and variance as of I_1 for texture synthesis. This is then decomposed to orientation subbands at each scale using the complex steerable pyramid. The set of features computed on the original image are sequentially imposed on the lowpass subband and the bandpass subbands in a recursive manner. This is the coarse to fine block in Figure 2.9. A lowpass image is simultaneously reconstructed in this step. The auto correlation, skew and kurtosis of the reconstructed lowpass image is then imposed on the synthesized image. The marginal statistics or pixel statistics are later imposed on the output of adding the lowpass image and the variance adjusted highpass band. The final synthesized image is obtained by repeating this whole procedure for a pre-determined number of iterations. Figure 2.9 shows the steps involved in the synthesis of the iris texture.

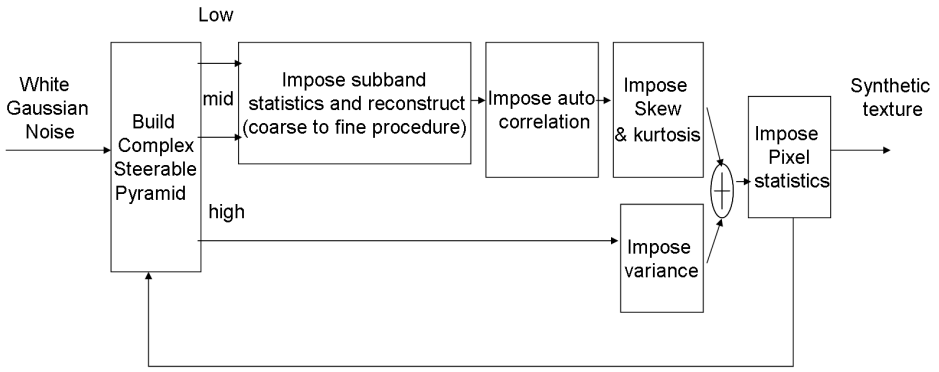

Figure 2.9: Block diagram for the synthesis of texture based on [7]

In the experiments the synthesis algorithm is repeated for 25 iterations. At each iteration the constraint is imposed such that the new image has not changed much from the original. This condition is imposed by moving in the direction of the gradient of the texture parameters measured, $\nabla\Phi_k(\overrightarrow{x})$, where $\overrightarrow{x}$ is the image from the previous iteration. The new texture at each iteration is thus obtained as follows:

$$\overrightarrow{x}^{(n)} = \overrightarrow{x}^{(n-1)} + \lambda_k \overrightarrow{\nabla}\Phi_k(\overrightarrow{x}^{(n-1)}),$$

Here λ_k is chosen such that,

$$\Phi_k(\overrightarrow{x}^{(n)}) = c_k.$$

Also in the experiments the number of scales (N) and orientations (K) used in constructing the steerable pyramid are 2 and 4, respectively. This results in 8 subbands. The spatial neighborhood (M) used is 5 x 5.

2.7 Creating cluster classes

Principal Direction Divisive Partitioning

PDDP [45] is an unsupervised hierarchical divisive method of clustering a set of sample data based on principal component analysis. It is a top down approach to clustering. In our case the input data to be clustered are the feature vectors extracted from each of the iris images in the database. A matrix F_{nXp} representing feature vector matrix for p subjects in the database with each feature vector of dimension 'n' is constructed to partition

the data. The feature set is considered as one whole entity and is recursively partitioned to two using the principal component analysis making the algorithm divisive. During the process a hierarchical partition structure is generated to represent each leaf node and the children partitions of a parent cluster. Each time the p samples are partitioned based on the principal component or direction which is the leading eigen vector of the covariance matrix of F_{nXp}. Each feature vector is projected on to the leading component $\mathbf{u}$ as,

$$\sigma \upsilon_i = \mathbf{u}^T(\mathbf{f}_i - \mathbf{w}),$$

$\mathbf{w}$ is the mean of the features in the matrix F and σ is a constant. A feature vector $\mathbf{f}_i$ in the parent node is partitioned to the left child node if its projection υ_i is ≤ 0 and right child node if $\upsilon_i > 0$. A feature vector is arbitrarily placed in the left node if its projection is zero. This is repeated until the desired number of clusters are obtained. At each iteration, the cluster with the highest scatter value or non cohesiveness is chosen to be partitioned. The sum of eigen-values is used as the measure of scatter or cohesiveness of a cluster. The higher the scatter value, higher is the cohesiveness and the cluster is chosen to be split into two.

2.8 Database

Experiments are performed on the datasets UPOL and CASIA V.3-Interval. UPOL dataset consists of 24 bit RGB color images for each of the 64 users with 3 samples per each eye. They are scanned using the TOPCON TRC50IA optical device connected to Sony DXC-950p 3CCD camera [46]. CASIA-IrisV3-Interval [47] dataset, collected by Chinese Academy of Sciences Institute of Automation (CASIA), consists of 8 bit gray scale images captured at near infrared illumination. The images are captured using the self developed camera by the Center for Biometrics and Security Research. The database consists of left and right eye images of 249 users. There are total of 192 images each of the left and right eye in UPOL database, and 1335 and 1320 images of the left and right eye in the CASIA-IrisV3-Interval database.

2.9 Iris pre-processing

Before feature extraction each of the iris images are subjected to image pre-processing. The preprocessing step includes, iris segmentation (localizing the two boundaries, pupil-iris boundary and iris-sclera boundary), iris normalization, and image enhancement. The localization of the two boundaries are performed either using the geodesic active contours [23, 48] or by manually segmenting the iris. The CASIA-IrisV3-Interval database is segmented using geodesic active contours and the UPOL database is segmented manually. Two circles are then fit to the localized boundaries. The parametric representation of the circle provides the center and radius of the circles, representing the center and radius of the pupil-iris boundary and the iris-sclera boundary, respectively. The segmented iris is then normalized using Daugman's rubbersheet model as discussed in chapter 1. The normalized images are enhanced using contrast-limited adaptive histogram equalization (CLAHE) technique. The image is tessellated to 64 tiles, and each tile is histogram equalized such that its original histogram distribution matches a uniform flat distribution. Each of the neighboring tiles are bi-linearly interpolated to remove the artificially induced boundaries.

The features of the UPOL database are computed on gray scale converted iris images. Red (R), green (G) and blue (B) components are of a colored image are converted to gray scale image (I) via,

$$I = 0.2989 * R + 0.5879 * G + 0.1140 * B$$

The segmented irises are normalized using the Daugman's rubbersheet model. The images in the UPOL database are normalized to size of 150 x 720 pixels. Images in the UPOL database are also normalized to size 64 x 360 pixels in order to compare the performance of proposed technique on iris rich in texture (UPOL at 64 x 360) and noisy database (CASIA-IrisV3-Interval at 64 x 360). The normalized irises of size 64 x 360 pixels is labeled as low resolution UPOL database for experimental purpose. Features from blocks of width 2^i, with $6 \leq i \leq 9$ on UPOL and $6 \leq i \leq 8$ on low resolution UPOL and CASIA-IrisV3-Interval database are extracted for the purpose of texture analysis as discussed in the following sections.

2.10 Experimental Evaluation

In order to evaluate the results of classification the database is split to two sets: train set and test set. The left irises are used for training and right irises for testing. Each of the iris images in both the sets are subjected to segmentation, normalization, enhancement, and feature extraction. The features of the train set are used to obtain the pre-determined cluster classes. Experiments are evaluated for number of clusters $n_c =$, 3 and 5. Figure 2.10 shows the examples of samples in each class.

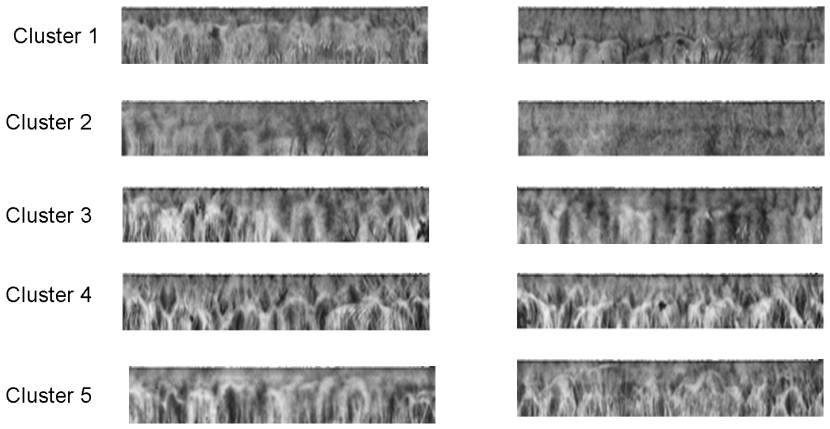

Figure 2.10: Examples of irises in the 5 clusters

The block location considered for test set is the same as the block location considered during the training phase of creating texture classes. The test set consists of multiple samples for each subject in the database. During testing a randomly selected sample of a subject is used to determine the class assigned to the subject. The remaining samples of the same subject are used for testing. In cases of subjects with only one sample, we do not use the subject in the test set. The classification is correct if the remaining samples of a subject are assigned to the same class as the first random sample. Figure 2.11 shows the way the experiments are evaluated. In order to evaluate the We perform decision level fusion and feature level fusion and evaluate the classification accuracies. The decision level two independent iris blocks are considered for testing and correct classification of iris using any of the blocks results in correct classification of the iris. On the other hand feature level fusion, fuses the features extracted from two iris blocks and performs classification.

As mentioned earlier the features extracted from the original and synthetic iris textures

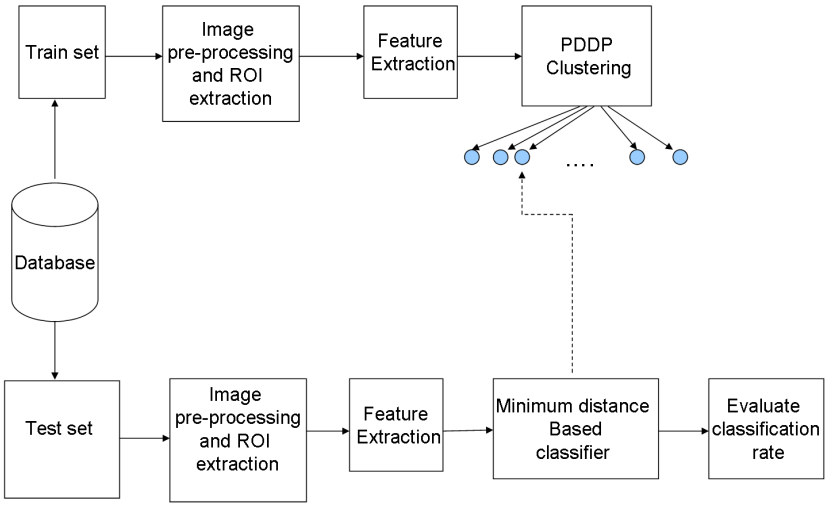

Figure 2.11: Our approach for iris classification

are classified based on minimum distance rule using centroid based classification scheme and K-Nearest Neighbor classification scheme. Three experiments are performed:

i. Classifying an iris using features from only one block of the iris.

ii. Feature level fusion: Classifying an iris by concatenating two feature sets extracted from two different blocks- One from the original iris and the other from another block of the original iris or from the synthetic image.

iii. Decision level fusion: Classifying an iris by performing independent classification on the features extracted from two blocks of same dimension. One set of features is from the original iris image and the other is either from the synthesized iris image or a different region from the original iris.

Figure 2.12 shows the outline of the three experiments conducted. Experiment I is shown in 2.12(a), experiment II is shown in 2.12(b) and experiment III is illustrated in 2.12(c).

The results of K-nearest neighbor classification scheme are not included as it performed equivalently to the centroid based classification scheme. It was observed that for experiments 2 and 3 the feature vector f_{synth} from the synthetic iris texture performed similarly as the feature from the original texture f_{orig}. the f_{synth} is similar to f_{orig} since

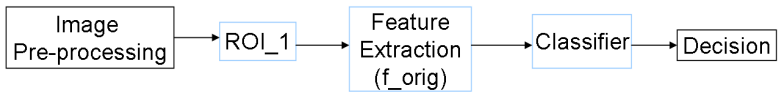

(a) Experimental setup for experiment I

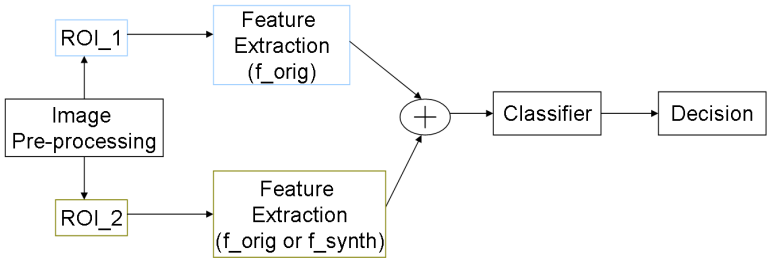

(b) Experimental setup for experiment II

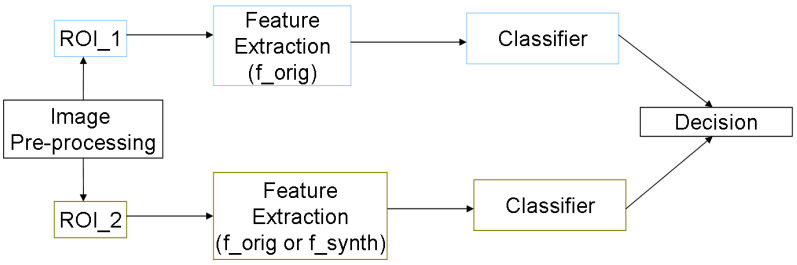

(c) Experimental setup for experiment III

Figure 2.12: Experimental Setups for experiment I 2.12(a), experiment II 2.12(b) and experiment III 2.12(c)

the synthesis of an image uses the criteria that the expected values of the constraints or features of the synthesized image is similar to the values, c_k of the original image. This is because the synthesis of texture was performed such that the textural features extracted both from original and synthesized texture are similar. For simplification these results are not included.

Experiment 1

In this experiment, the features from each block of the original texture are considered for classification. A set of blocks with the same width are numbered incrementally starting from 1. The numbering of blocks proceeds from left to right of the normalized iris. The accuracy of the classifier is evaluated for features from each block. Following are the results on UPOL, low resolution UPOL and CASIA-IrisV3-Interval database for 3 and 5 clusters.

The following tables show the results of classification for each of the blocks with different column sizes or widths.

Table 2.1 has the results for experiment 1 on the UPOL database, which are classified by comparing the query feature vector with centroids of clusters. This is done for a predetermined number of 3 and 5 clusters. Table 2.2 shows the results of classification on the low resolution UPOL database and Tables 2.3 shows the results on the CASIA-Irisv3-interval database.

Experiment 2

The features from two different blocks ($\mathbf{f}_{B1}$, $\mathbf{f}_{B2}$), are fused to form one feature vector $\mathbf{f}_{B1B2}$. Training and testing is performed on the fused feature sets. Experiments are performed on all three databases. The performance on feature level fusion did not show any improvement over the results of classification using just one block and is therefore redundant. Thus results on UPOL database are not included.

Tables 2.4, 2.5 show the results for top 3 classification accuracies obtained for combination of two features for the classification of iris texture on low resolution UPOL databse for 3 and 5 clusters respectively. Results for CASIA-IrisV3-Interval database is shown in 2.6, 2.7

Table 2.1: Exp1 : Results of classification experiment to 3 and 5 clusters using features extracted from each of the iris blocks from the UPOL database

Region number	Number of clusters, n_c	
	$n_c = 3$	$n_c = 5$
Column size 64		
1	87.50	78.91
2	**89.84**	78.13
3	85.94	82.03
4	83.60	**86.72**
5	79.69	75.00
6	88.28	75.78
7	82.81	78.91
8	82.81	79.69
9	80.47	79.69
10	73.44	72.66
11	87.50	78.91
12	88.28	85.16
13	78.91	66.41
14	83.60	75.00
15	71.88	65.63
16	75.78	66.41
17	78.91	71.09
18	67.19	67.19
19	77.34	69.53
20	75.78	69.53
21	82.03	78.91
Column size 128		
1	**92.18**	82.03
2	85.16	**82.81**
3	90.63	78.91
4	84.38	78.13
5	88.28	81.25
6	84.38	77.34
7	73.44	71.88
8	75.00	72.66
9	78.12	69.53
10	79.69	64.84
Column size 256		
1	87.50	**84.38**
2	**91.41**	79.69
3	83.59	72.66
4	72.66	64.84
Column size 512		
1	85.16	**78.91**
2	**85.94**	69.53

Table 2.2: Exp1 : Results of classification experiment to 3 and 5 clusters using features extracted from each of the iris blocks from the low resolution UPOL database

Region number	Number of clusters, n_c	
	$n_c = 3$	$n_c = 5$
Column size 64		
1	**92.18**	**85.15**
2	88.28	78.90
3	87.50	84.37
4	85.15	83.59
5	81.25	75.00
6	82.03	71.88
7	83.60	72.66
8	77.34	69.53
9	78.13	70.31
10	79.69	73.44
Column size 128		
1	**90.63**	**78.91**
2	82.81	73.44
3	75.78	73.44
4	83.60	74.22
Column size 256		
1	78.91	**75.78**
2	**82.03**	66.41

Table 2.3: Exp1 : Results of classification experiment to 3 and 5 clusters using features extracted from each of the iris blocks from the CASIA-IrisV3-Interval database

Region number	Number of clusters, n_c	
	$n_c = 3$	$n_c = 5$
Column size 64		
1	61.50	50.45
2	62.66	49.29
3	**66.31**	43.85
4	60.87	45.81
5	56.51	51.43
6	63.81	52.41
7	65.33	52.32
8	64.71	48.84
9	65.86	51.88
10	64.62	**54.19**
Column size 128		
1	56.51	46.08
2	58.82	51.78
3	64.44	**52.14**
4	**65.78**	51.69
Column size 256		
1	**66.49**	**53.12**
2	64.35	53.03

Table 2.4: Exp2 : Results of classification of low resolution UPOL database to 3 clusters. The features of two blocks are fused before classification

Column size 64			
ROI_2/ROI_1	1	3	2
1	-	-	-
2	**85.16**	-	-
3	80.47	75.78	-
4	78.91	75.78	-
5	77.34	79.69	68.75
6	76.56	78.12	60.94
7	78.12	**82.81**	76.56
8	79.69	82.03	69.53
9	76.56	73.44	74.22
10	81.25	77.34	**82.81**
Column size 128			
ROI_2/ROI_1	1	3	2
1	-	-	-
2	72.66	-	-
3	78.12	-	**68.75**
4	**78.91**	**78.12**	60.16
Column size 256			
ROI_2/ROI_1	1		
1	-		
2	**79.69**		

Table 2.5: Exp2 : Results of classification of low resolution UPOL database to 5 clusters. The features of two blocks are fused before classification

Column size 64			
ROI_2/ROI_1	1	2	4
1	-	-	-
2	87.50	-	-
3	82.81	-	85.94
4	**92.19**	85.94	83.59
5	89.84	85.16	77.34
6	83.59	82.03	84.38
7	78.91	73.44	85.94
8	84.38	78.91	82.81
9	77.34	78.12	82.81
10	82.03	**89.84**	**87.50**
Column size 128			
ROI_2/ROI_1	1	3	2
1	-	-	-
2	**89.84**	-	-
3	82.03	-	**82.03**
4	79.69	**83.59**	66.41
Column size 256			
ROI_2/ROI_1	1		
1	-		
2	**85.94**		

Table 2.6: Exp2 : Results of classification of CASIA-IRISV3-Interval database to 3 clusters. The features of two blocks are fused before classification

Column size 64			
ROI_2/ROI_1	7	4	2
1	-	-	-
2	-	-	-
3	-	-	60.52
4	-	-	57.22
5	-	56.60	56.68
6	-	62.66	63.46
7	-	60.07	61.94
8	**67.74**	**66.84**	**66.67**
9	61.14	63.19	63.19
10	63.37	62.03	65.51
Column size 128			
ROI_2/ROI_1	3	2	1
1	-	-	-
2	-	-	**58.91**
3	-	59.98	55.35
4	**62.83**	**61.59**	59.54
Column size 256			
ROI_2/ROI_1	1		
1	-		
2	**57.22**		

Table 2.7: Exp2 : Results of classification of CASIA-IRISV3-Interval database to 5 clusters. The features of two blocks are fused before classification

Column size 64			
ROI_2/ROI_1	8	9	5
1	-	-	-
2	-	-	-
3	-	-	-
4	-	-	-
5	-	-	-
6	-	-	**54.01**
7	-	-	51.25
8	-	-	51.16
9	52.67	-	53.03
10	**55.53**	**55.08**	51.07
Column size 128			
ROI_2/ROI_1	3	1	2
1	-	-	-
2	-	46.08	-
3	-	**50.18**	**50.00**
4	**51.87**	46.26	49.73
Column size 256			
ROI_2/ROI_1	1		
1	-		
2	**51.16**		

Experiment 3

Here features from two different blocks are classified independently. That is, each iris block from a users normalized iris undergoes testing phase independently. A texture is considered to be correctly classified if either of the test features from two different blocks of the same user are labeled to the class the users first sample was assigned. For example, consider two iris blocks from a subjects first sample used for class assignment have two feature vectors ($\mathbf{U}_{tr1}$, $\mathbf{U}_{tr2}$), and the blocks from a test sample have feature vectors ($\mathbf{U}_{te1}$, $\mathbf{U}_{te2}$) respectively. If the random features are assigned to class A and B during class determination for the user, then the test features are correctly classified if either $\mathbf{U}_{te1}$ is assigned to class A or $\mathbf{U}_{te2}$ is assigned to class B. Here, the classification accuracy for combinations of different blocks with same widths is evaluated. In the tables, ROI_1 and ROI_2 correspond to the location from which the blocks are extracted for the purpose of classification. The results are provided for the top 3 combinations of blocks for classification. The '-' represent no classification is done for those regions as they are redundant in the evaluation of classification accuracy.

Tables 2.8, 2.9 show the results of classification for 3 and 5 clusters on the UPOL database. The two features used are from two different blocks of the original texture. Table 2.10, 2.11 show the results of classification on the low resolution UPOL database and Table 2.12, 2.13 show the results of classification on the CASIA-IrisV3-Interval database for 3 and 5 clusters respectively.

2.11 Analysis of Experimental Results

The goal of experiment1 was to determine if regions with smaller widths can be used for the purpose of classification. It is observed from all three databases that we obtain comparable classification accuracies for blocks with different widths. Apart from this it is also observed that performance either remains constant or decreases with increasing widths. The classification accuracies for 5 clusters with width 64 shows that the regions with low performance could be due to the noisy regions such as eyelids and eyelashes. This shows that in case of a noisy database it helps to perform classification by extracting features from regions corresponding to iris texture. Figure 2.13 illustrates an example of the normalized UPOL, low-resolution UPOL and the CASIA-IrisV3-Interval database.

Table 2.8: Exp3 : Results of classification of UPOL database to 3 clusters. Each block is classified independently

Column size 64			
ROI_2/ROI_1	7	1	2
1	-	-	-
2	-	96.88	-
3	-	96.88	98.44
4	-	98.44	96.09
5	-	96.88	**99.22**
6	-	98.44	98.44
7	-	96.88	98.44
8	99.22	**99.22**	99.22
9	96.09	97.66	97.66
10	90.63	92.97	96.88
11	**100.00**	99.22	98.44
12	100.00	99.22	98.44
13	92.97	94.53	98.44
14	96.88	98.44	97.66
15	94.53	98.44	94.53
16	93.75	96.09	96.09
17	92.19	97.66	98.44
18	93.75	96.88	98.44
19	96.88	95.31	95.31
20	92.19	96.88	98.44
21	97.66	94.53	95.31
Column size 128			
ROI_2/ROI_1	1	3	2
1	-	-	-
2	96.88	-	-
3	**100.00**	-	**99.22**
4	99.22	96.09	98.44
5	98.44	99.22	96.09
6	99.22	96.09	95.31
7	98.44	96.88	94.53
8	98.44	98.44	96.09
9	99.22	**100.00**	97.66
10	96.88	99.22	92.19
Column size 256			
ROI_2/ROI_1	2	1	3
1	-	-	-
2	-	**96.88**	-
3	96.88	95.31	-
4	**97.66**	96.09	**91.41**
Column size 512			
ROI_2/ROI_1	1		
1	-		
2	**93.75**		

Table 2.9: Exp3 : Results of classification of UPOL database to 5 clusters. Each block is classified independently

Column size 64				
ROI_2/ROI_1	3	4	5	2
1	-	-	-	-
2	-	-	-	-
3	-	-	-	92.19
4	97.66	-	-	95.31
5	93.75	96.88	-	96.10
6	**99.22**	95.31	92.97	96.10
7	97.66	96.88	93.75	91.41
8	97.66	95.31	96.88	96.10
9	96.88	97.66	96.10	95.31
10	96.88	94.53	91.41	96.10
11	98.44	94.53	94.53	96.88
12	96.10	96.88	**98.44**	96.88
13	92.19	**98.44**	94.53	91.41
14	96.10	93.75	92.19	92.97
15	96.88	92.97	91.41	92.19
16	91.41	95.31	90.63	92.19
17	95.31	94.53	89.84	92.97
18	94.53	92.97	92.97	94.53
19	96.88	97.66	93.75	**97.66**
20	94.53	94.53	92.97	94.53
21	96.88	96.10	93.75	96.88

Column size 128				
ROI_2/ROI_1	1	2	3	4
1	-	-	-	
2	**97.66**	-	-	
3	91.41	95.31	-	
4	94.53	95.31	92.97	
5	95.31	94.53	**96.09**	
6	96.88	**96.88**	96.09	
7	95.31	94.53	96.094	
8	94.53	91.41	92.19	
9	90.63	93.75	91.41	
10	94.53	94.53	92.19	

Column size 256			
ROI_2/ROI_1	1	2	3
1	-	-	-
2	92.97	-	-
3	**94.53**	90.62	-
4	92.19	**92.19**	88.28

Column size 512	
ROI_2/ROI_1	1
1	-
2	**87.5**

Table 2.10: Exp3 : Results of classification of low resolution UPOL database to 3 clusters. Each block is classified independently

Column size 64			
ROI_2/ROI_1	3	1	2
1	-	-	-
2	-	98.44	-
3	-	**99.22**	**98.44**
4	**100.00**	98.44	97.66
5	96.88	99.22	98.44
6	98.44	96.88	96.88
7	98.44	96.88	99.22
8	97.66	98.44	96.09
9	97.66	93.75	96.09
10	98.44	98.44	96.88
Column size 128			
ROI_2/ROI_1	1	2	3
1	-	-	-
2	**99.22**	-	-
3	96.88	**98.44**	-
4	98.44	96.09	**95.31**
Column size 256			
ROI_2/ROI_1	1		
1	-		
2	**96.09**		

Table 2.11: Exp3 : Results of classification of low resolution UPOL database to 5 clusters. Each block is classified independently

Column size 64			
ROI_2/ROI_1	1	2	3
1	-	-	-
2	96.09	-	-
3	**97.66**	92.97	-
4	95.31	**96.09**	93.75
5	96.88	93.75	**96.09**
6	94.53	92.97	93.75
7	92.19	92.19	92.19
8	90.63	90.63	94.53
9	92.97	93.75	95.31
10	93.75	96.09	96.09
Column size 128			
ROI_2/ROI_1	1	2	3
1	-	-	-
2	**96.09**	-	-
3	93.75	**95.31**	-
4	93.75	90.63	**89.06**
Column size 256			
ROI_2/ROI_1	1		
1	-		
2	**87.50**		

Table 2.12: Exp3 : Results of classification of CASIA-IrisV3-Interval database to 3 clusters. Each block is classified independently

Column size 64			
ROI_2/ROI_1	1	2	6
1	-	-	-
2	84.58	-	-
3	**88.77**	**86.45**	-
4	86.36	85.65	-
5	81.99	83.87	-
6	84.67	85.03	-
7	86.54	86.45	85.47
8	84.58	88.50	**87.25**
9	83.24	85.91	86.63
10	84.04	85.65	86.90
Column size 128			
ROI_2/ROI_1	3	1	2
1	-	-	-
2	-	74.51	-
3	-	**84.58**	81.91
4	**84.76**	84.31	**84.22**
Column size 256			
ROI_2/ROI_1	1		
1	-		
2	**81.02**		

Table 2.13: Exp3 : Results of classification of CASIA-IrisV3-Interval database to 5 clusters. Each block is classified independently

Column size 64			
ROI_2/ROI_1	2	6	7
1	-	-	-
2	-	-	-
3	69.61	-	-
4	68.36	-	-
5	74.78	-	-
6	**78.2531**	-	-
7	76.92	72.73	-
8	74.42	75.58	72.73
9	75.76	76.29	**76.56**
10	76.47	**76.92**	75.31
Column size 128			
ROI_2/ROI_1	1	3	2
1	-	-	-
2	65.95	-	-
3	71.39	-	71.84
4	**75.04**	**75.04**	**72.10**
Column size 256			
ROI_2/ROI_1	1		
1	-		
2	**72.91**		

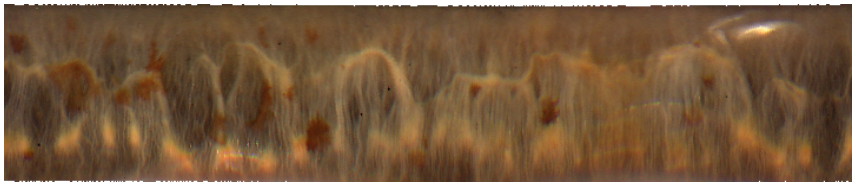

(a) UPOL

(b) low-resolution UPOL

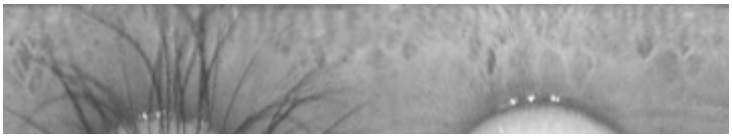

(c) CASIA-IrisV3-Interval

Figure 2.13: Examples of normalized iris images in the database

In order to understand the performance of the algorithm on a low resolution database, images in the UPOL database are downsampled to the size of images in the CASIA-IrisV3-Interval database. It is observed that with the decreasing resolution, the classification accuracy decreases. A similar trend is observed in all three experiments.

In the case of experiment 2 (Feature level fusion) the maximum accuracy achieved by fusing features extracted from blocks of irises of similar widths is lesser than the maximum accuracy accomplished using just one iris block. This could be accounted to decrease in discriminativeness due to direct fusion of features.

For experiment 3 (decision level fusion) it is clearly seen that fusing the result of classification of an iris sample at the decision level using two different blocks increases the performance to a large extent. The advantage of performing independent classification is that we take advantage of features from two different blocks which may be discriminative. It is observed that the classification accuracies achieved using decision level fusion is equal to or higher than the maximum accuracy achieved using only one region for classification. Further analysis and experimentation is required to find which iris blocks result in better classification.

2.12 Summary and future work

The experiments show a promise in grouping iris texture based on statistical texture analysis and are successful in correctly assigning samples of an iris to a cluster. The above experiments show that small iris blocks can be used for the purpose of iris texture classification. It is also observed that the resolution of the original iris image and size of the blocks considered for feature extraction affect the classification accuracy. Also the experiments to some extent show that the classification performance decreases when using blocks of iris containing noise such as eyelashes and eyelids, compared to block containing only the iris texture.

Other types of analysis can be performed for texture classification using the proposed method:

a In experiment 1, though UPOL database is of high resolution and the iris is not occluded due to eyelids and eyelashes, very high classification rates were not observed. One reason

could be due to down sampling the ROI for computational purpose. The iris texture classification can be analyzed at more scales and at higher resolution resulting in feature vectors of higher dimensions.

b Though we observe that the blocks of iris with no occlusion give better performance, it is required to probe into the reason for difference in performance for different blocks of same width and identify the best ROI for iris classification.

c Further analysis can be performed on feature selection in the feature level fusion for better performance in grouping iris texture.

Chapter 3

Detection of Macro Features

3.1 Introduction

Figure 3.1 illustrates the biometric recognition using indexing.

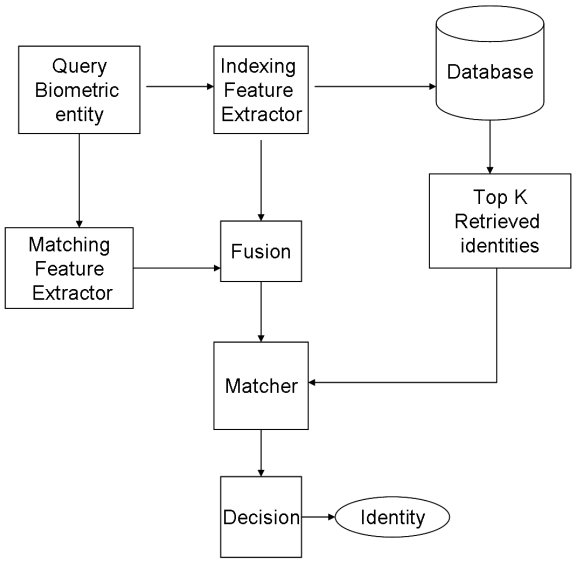

Figure 3.1: Identification using indexing

Rajiv Mukherjee [34, 35] in his work, discussed some of the iris indexing techniques where iris texture is analysed to retrieve a small number of identities from the database for the purpose of identifying the query image. This work explores anatomical structures of the iris, such that detection and characterization of the anatomical structures referred

to macro features may provide a novel set of features for iris recognition and indexing or image retrieval.

Iris characteristics such as pigmentation spots, nevi, and freckles as discussed in Chapter 1 are the macro features proposed to be detect. The successful detection and representation of these macro features may provide a new set of landmark or minutiae points, which can be used for iris recognition (by obtaining corresponding minutiae points between two images) and to retrieve only those images from the database which have these macro features at a certain location with certain characteristics. Figure 3.2 shows an example of the macro features proposed to be detected and characterized using centroids.

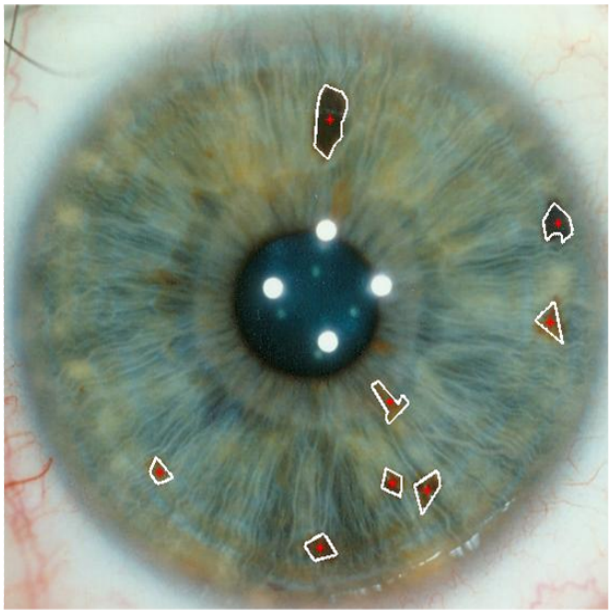

Figure 3.2: Example of macro features

In this thesis we look at anatomical structures of the iris. The features such as freckles, nevi and other pigmentation features such as sectoral heterochromia in the iris are referred to as macro features. These features are usually not permanent and are observed in patients from the age group of 40 [13], yet these may be sufficient enough to differentiate two irises with macro features at different locations in iris and with different characterization. In addition these structures are not present in every iris giving the advantage for use in image retrieval based on these macro features. For the purpose of recognition or image retrieval these features first need to be detected in an iris. Characteristics and challenges associated with the detection of macro features may provide better understanding of the

techniques used for the purpose of detection.

3.1.1 Characteristics of macro features

The detection approaches can better be handled by understanding the characteristics of these macro features in terms of image processing. High resolution color images are used in this thesis.

- Size - The macro features vary in size from the order of few tens of pixels to thousands of pixels.
- Color - The color of the macro features within a single iris is not constant. The macro features usually are characterized with colors from light orange, yellow to dark brown.
- Texture - Unlike the texture of moles and blob like structures, the texture within the area of the feature of interest is not always homogeneous. The texture also varies across macro features within the same iris and across different irises. But texture is usually smooth and pigmented compared to the iris texture.
- The color and texture of macro features is similar to texture of other iris characteristics such as pupillary frill, crypts. Also the color and texture of macro features is similar to the color and texture of other colored irises. For example, some macro features are similar in color and texture to certain brown colored irises.
- Compared to blue colored irises, the contrast between brown colored iris texture and a potential macro feature is low.

Due to these characteristics of the macro features, traditional image processing detection techniques fail to detect and localize the macro features. Following are some of the challenges associated with the detection techniques.

Challenges associated with the detection techniques for macro features

1. Texture based detection of macro features : Many regions in the iris have the same texture and intensity as the macro features, for example, the pigmented anterior

layer exposed due to crypts and the pupillary frill. In addition it is not possible to eliminate erroneous regions detected based on size due to the variable size and shape of the macro features.

2. Traditional edge detection based on intensity : The iris is a highly textured image as can be observed by the scales defined by Mats Larsson [19] to classify iris. With the change in texture of iris, distinguishing the edges of macro features from the edges in the iris gets complicated. Increase in complexity to distinguish the edges associated with macro features from the spurious edges due to radial furrows and crypts can be observed for blue eyes (refer to figure 3.3). In the case of brown eyes it is observed that due to low contrast the edge detection algorithms fail.

The rest of this chapter discusses the approaches studied and evaluated for the purpose of detection of macro features from the textured iris background. Also the ability of partial iris matching using multi-scale local minutiae points is demonstrated. Furthermore the ability of macro features to perform image retrieval is discussed.

3.2 Proposed approach

The macro features correspond to either small regions in the iris or regions corresponding to a sector in the iris. The macro features typically correspond to image discontinuities such as color, texture and intensity. We propose to extract regions corresponding to the image discontinuities due to color, texture and intensity, but due to the presence of other anatomical structures such as crypts and radial furrows, spurious detections are obtained. Finally classification is performed to obtain detections corresponding only to the macro features. Features are extracted from the neighborhood of the detections for the purpose of classification.

Due to the variable factors such as size, texture and shape, we propose two approaches namely region based approach and multi-scale approach. In the region based approach, an iris image is partitioned to small regions based on image discontinuities and select few regions corresponding to high magnitude of image discontinuity. On the other hand, multi-scale approach detects local feature points or extremum points corresponding to image discontinuities of different sizes. Features extracted from the regions selected or a

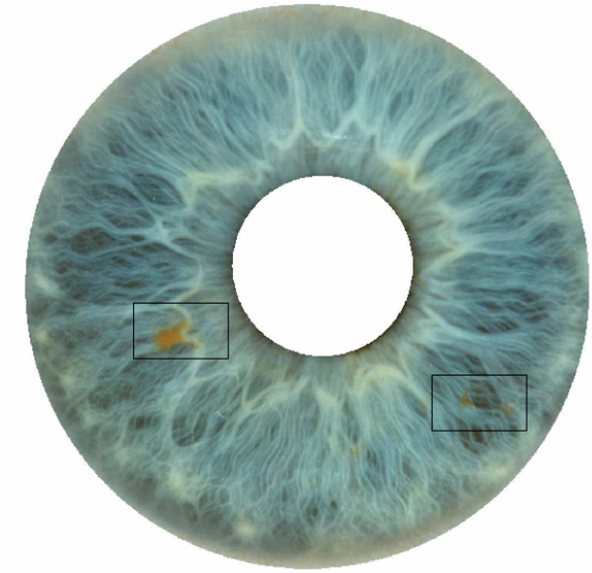

(a)

(b)

Figure 3.3: Example of (a) blue iris (rich in texture), (b) brown iris (low contrast iris)

local neighborhood around the extremum points are subjected to unsupervised clustering in order to classify image discontinuities detected due to macro features from spurious features.

3.3 Feature Extraction

Feature extraction is the process of extracting discriminating features for each of the detections obtained. Due to the non-homogeneous nature of iris texture we have regions corresponding both to the macro features and regions belonging to iris texture. The features that are extracted from each of these regions are color, statistical textural features computed directly on the gray scale image or from filtered responses of the image as discussed in chapter 2. Some of the statistical features computed for a region with L possible intensity levels represented with the random variable z_i and the pixel intensity histogram p(z) are:

$$Mean, m = \sum_{i=0}^{L-1} z_i p(z_i)$$

$$\text{Standard deviation } \sigma = \sqrt{\mu_2(z)} = \sqrt{\sigma^2}, \qquad \mu_2 \quad \text{is the second moment}$$

$$\text{Smoothness } R = 1 - \frac{1}{(1+\sigma^2)}$$

$$\text{Third-moment } \mu_3 = \sum_{i=0}^{L-1} (z_i - m)^3 p(z_i)$$

$$\text{Uniformity } U = \sum_{i=0}^{L-1} p^2(z_i)$$

$$\text{entropy } e = -\sum_{i=0}^{L-1} p(z_i) \lg_2 p(z_i)$$

The above textural measures can be computed on the gray scale image along with other higher order moments. The mean - measures the average intensity, standard deviation - measures the average contrast, R - measures the smoothness of a region and is zero for regions with constant intensity and 1 for regions with large excursions, third moment - measures the skewness of the histogram, uniformity measures the uniformness in a region

and is maximum when all gray levels in a region are constant, and the entropy measures the randomness in a region. A subset of these textural measures or the entire set of textural features extracted may be used for classification.

3.4 Region Based Approach

3.4.1 EdgeFlow based segmentation

Segmentation is the process of partitioning an image to indexed region map such that, each region is homogeneous in terms of the features or attributes describing the region, and that each region has well defined boundaries. Traditional segmentation algorithms are based on texture or grayscale images. The images are segmented using the gradient of an image (discontinuities in intensity), unsupervised clustering of pixels or by characterizing the texture and classifying the texture to different classes. The texture features are usually computed on grayscale images or filtered outputs of an image as described in chapter 2. The pigmentation features desired to be captured have different pigmentation from the color of the iris and in some cases different texture from the iris. We choose to segment images using both color and texture features according to [49]. The boundaries of indexed regions are not detected from the gradient of an image. The boundaries are rather detected indirectly by computing the flow direction at each pixel location pointing to the nearest boundary and then localizing boundaries at locations that encounter opposing directions of edge flows. Edge flow vector is defined at each pixel location using a predictive model identifying the direction of change of color and texture attributes at a given scale σ, where σ is the user input defining the resolution at which the boundary detection and image segmentation is performed. An edge flow in general at an image location 's' with an orientation θ is defined as:

$$F(s,\theta) = F[E(s,\theta), P(s,\theta), P(s,\theta+\pi)], \quad where$$

1. E(s,θ) is the edge energy at location 's' along the orientation 'θ', measuring the energy corresponding to the change of local image information with respect to color or texture.

2. P(s, θ) is the probability of finding the image boundary if the corresponding flow at

location 's' flows in the direction of 'θ'.

3. P(s, $\theta + \pi$) is the probability of finding image boundary if the flow at location 's' is in the opposite direction ($\theta + \pi$).

The edge energy is computed for each of the attributes considered namely, color and texture at each pixel location and is iteratively propagated to the neighboring pixels if they have the same direction of flow. A region boundary is detected if two image locations have opposite direction of edgeflows.

In order to compute the edge flow vectors, the edge energies are computed from filtered responses of image I(x,y) for each attribute. The intensity edge flow is computed as the magnitude of the gradient of the Gaussian smoothed image $I_\sigma(x, y)$ along the orientation θ at scale σ.

$$E(s, \theta) = \left| \frac{\partial}{\partial \mathbf{n}} [I(x, y) * G_\sigma(x, y)] \right| = |I(x, y) * GD_{\sigma,\theta}(x, y)| = |I_\sigma(x, y)|$$

Here 's' is the location (x,y) and n is the unit vector in the direction of the gradient. The probability of finding the nearest boundary is computed for two directions namely θ and $\theta + \pi$ at location 's' for each of the edge energies along the orientation θ. The probabilities are computed from the prediction errors of the neighbors at location 's' in the direction θ. That is the neighbors in the direction θ should have similar intensity if they belong to the same object, and higher the prediction error in a direction θ higher is the probability of finding a boundary in that direction. The prediction error and probabilities of edge flow direction along θ at a prediction distance d, such that $d = 4\sigma$, are computed as follows,

$$Error(s, \theta) = |I_\sigma(x + dcos\theta, y + dsin\theta) - I_\sigma(x, y)| = |I(x, y) * DOOG_{\sigma,\theta}(x, y)|$$

$$P(s, \theta) = \frac{Error(s, \theta)}{Error(s, \theta) + Error(s, \theta + \pi)}$$

Difference of offset Gaussian (DOOG), is the difference between two Gaussian convoluted images separated by a constant 'd'. Texture edge flow is computed on the same lines. The texture is captured from the image decomposition using bank of Gabor filters. The bank of Gabor filters are generated according to the scale parameter provided by the user. The lowest frequency U_l of the Gabor filters is set to $\frac{1}{4\sigma}$ cycles/pixel and the highest

U_h is set to 0.45 cycles/pixel. The mother complex Gabor filter is defined as,

$$g(x,y) = \left(\frac{1}{2\pi\sigma_x\sigma_y}\right)\exp\left[-\frac{1}{2}\left(\frac{x^2}{\sigma_x^2}+\frac{y^2}{\sigma_y^2}\right)\right]\cdot\exp[2\pi jWx], \qquad \text{with W} = U_h$$

A bank of Gabor filters is obtained by appropriate dilations and rotations of $g(x,y)$ using,

$$g_{mn}(x,y) = a^{-m}g(x',y'), \qquad \text{with a>1, and m,n = integer}$$

$$x' = a^{-m}(xcos\theta + ysin\theta),$$

$$y' = a^{-m}(-xsin\theta + ycos\theta),$$

with $\theta = \frac{n\pi}{K}$ and K is the total number of orientations, $a = (U_h/U_l)^{\frac{1}{S-1}}$ and S is the total number of scales in the multi resolution decomposition and $m = 0, 1, ...S-1$.

The images are decomposed using the Gabor filter bank such that $I(x,y) * g_i(x,y) = m_i(x,y)\exp[\phi_i(x,y)]$, where $1 \leq i \leq N$, and $N = S.K$ is the total number of filters. $m_i(x,y)$ is the amplitude of the subbands at each location (x,y). The texture edge energy measuring the change in local texture information is given by,

$$E(s,\theta) = \sum_{1\leq i\leq N} |m_i(x,y) * GD_{\sigma,\theta}(x,y)| \,.w_i$$

where $w_i = 1/\|\alpha_i\|$ and $\|\alpha_i\|$ is the total energy of the subband 'i'. The probabilities of the direction of edgeflow are computed from the weighted sum of the prediction errors at each location (x,y) from each of the subbands:

$$Error(s,\theta) = \sum_{1\leq i\leq N} |m_i(x,y) * DOOG_{\sigma,\theta}(x,y)| \,.w_i,$$

$$P(s,\theta) = \frac{Error(s,\theta)}{Error(s,\theta) + Error(s,\theta+\pi)}$$

The edge flows from each attribute are combined to form a single edge flow vector. In case of color images the intensity edge flow is computed on each of the color bands and the texture edge flow is computed on the illuminance component, which is the average of

all three subbands. The single edge flow is obtained as,

$$E(s,\theta) = \sum_{a \in A} E_a(s,\theta).w(a), \text{ and } \sum_{a \in A} w(a) = 1$$

$$P(s,\theta) = \sum_{a \in A} P_a(s,\theta).w(a)$$

where a is the image attributes color, texture and $E_a(s,\theta)$ and $P_a(s,\theta)$ are the edge energy and the probability of edge flow at location 's' along direction 'θ' obtained from each attribute considered for the purpose of segmentation. For an image the edge flow vector at each location is computed along direction ranging from 0 to π, that is $\{F[E(s,\theta), P(s,\theta), P(s,\theta+\pi)]|_{0 \leq \theta < \pi}\}$. The final set of edge flow direction to be searched for nearest boundary at each location 's' is obtained by identifying a continuous range of flow directions which maximizes the sum of probabilities in the half plane considered, that is

$$\Theta(s) = \arg\max_{\theta} \left\{ \sum_{\theta \leq \theta' < \theta+\pi} P(s,\theta') \right\}$$

and the final edge flow F at the location 's' is given as a vector sum of edge flows at location 's' along the continuous range of directions identified such that the magnitude represents the edge energy and angle represents the flow direction,

$$F(s) = \sum_{\Theta(s) \leq \theta < \Theta(s)+\pi} E(s,\theta).exp(j\theta)$$

The edge flows at each location are propagated iteratively to the neighboring pixel in the direction of edge flow if both the pixels under consideration have similar flow direction which is an angle less than 90 degrees. Once the edge flows reach a stable state, the edges are identified at pixel locations which have two edge flows opposing each other, resulting in disconnected edges. A boundary connection and region merging algorithm is used to obtain final indexed regions which are homogeneous in terms of the attributes considered for the purpose of segmentation according to [49]. Figure 3.4 shows the result of performing edge flow based segmentation and its corresponding indexed map on normalized iris.

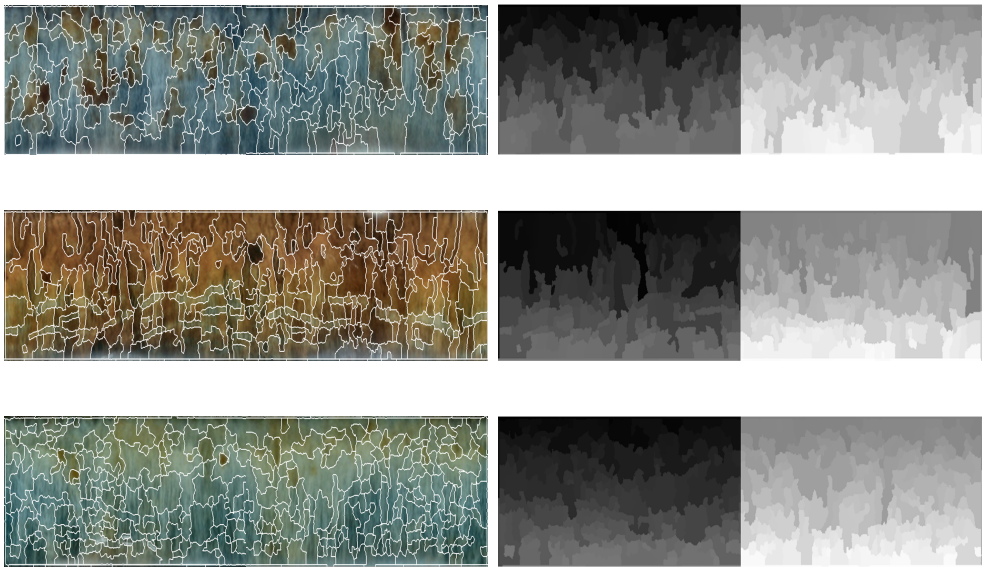

Figure 3.4: Left: Result of edgeflow based over segmentation on each normalized iris, Right: Corresponding indexed segmentation map

The next section provides a brief introduction on detection of image discontinuities using intensity edge detection and the extension of edge detection to colored images.

3.4.2 Color edge detection

Edge detection is the process of detecting image discontinuities. The visual discontinuities observed could be due to intensity or texture. The discontinuities are measured directly on grayscale in case of intensity or from filtered responses of image in case of texture. Some of the ways in which textural discontinuities have been measured are with the use of textural filters such as laws filter, discrete wavelet transforms (DWT), Gabor filters. The filtered responses are subjected to any classifier in order to obtain segmented regions or are subjected to boundary detection technique as mentioned in the previous section. In case of measuring intensity based discontinuities the grayscale image is subjected to filters for example directional edge operators such as Roberts filter, Prewitt filter at 0, 45, 90, 135, 180, 225, 270, 315, 360 degrees. These filters measure the intensity difference between center pixel of the filter and pixels spaced at a distance of 'd' pixels in each of the direction considered. Shown in Tables 3.1, 3.2 are examples of Sobel and Prewitt's filter at 0 and 90 degrees measuring the intensity difference between pixels around the

center pixel in the horizontal and vertical direction spaced at a distance of one pixel from the center pixel.

Table 3.1: Sobel filter

-1	-2	-1
0	0	0
1	2	1

-1	0	1
-2	0	2
-1	0	1

Table 3.2: Prewitt filter

-1	-1	-1
0	0	0
1	1	1

-1	0	1
-1	0	1
-1	0	1

The edge detection is computed at the center pixel as a result of convolution of the filter with the image. These filters can be extended to compute the pixel differences in all directions such as 0, 45, 90, 135, 180, 225, 270, 315, 360 degrees as shown in Table 3.3. Table 3.3 computes pixel differences between two pixels which are spaced one pixel apart. But it can be extended to compute pixel differences between two pixels space d pixels apart in the 8 directions. The edge detector then can be defined as,

$$edge = \max_{i=1..8}(X_0 - X_i)$$

where X_0 is the center pixel at which the edge is computed and X_i are the 8 neighboring pixels.

Table 3.3: Filter measuring the difference for the 8 neighbors

-1	-1	-1
-1	1	-1
-1	-1	-1

These filters are applied on grayscale images. These can be extended to color images or indexed images. Indexed images can be visualized as a stack of multiple grayscale

components. For example an RGB color image is an indexed image with red, green and blue representing each component of an indexed image. Each pixel in an indexed image is represented as I(x,y,z) where 'z' represents the indexed component and (x,y) provide the spatial coordinates of a pixel in the indexed component. Figure 3.5 shows the arrangement of an indexed RGB image of size 5 x 5 x 3, where 3 indicates the three components of an RGB image.

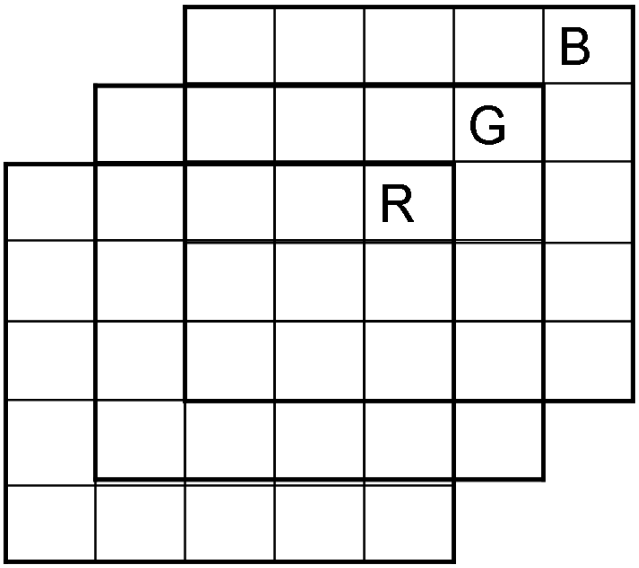

Figure 3.5: Indexed RGB image

Other examples of indexed images are Lab, HSV, HSI. These are color models which measure the color information. Each of the color spaces can be obtained directly from the (sRGB) standard RGB or from other colorspaces. sRGB is the color model used for computer based applications. CIE Lab color space is obtained from the CIE XYZ colorspace derived from the sRGB image. L measures the luminosity and a, b measure the variations of red versus green and yellow versus blue. Hue Saturation Value (HSV) color space is derived directly from the sRGB image. Hue measures the pure color value ranging from 0-360 and saturation measures the intensity of the color varying from 0-1, and value measures the brightness with 0 representing black and 1 representing the brightness or the saturated color. CIE lab and HSV colorspaces are obtained as follows [50],

If RGB are the components of sRGB then the normalized [rgb] components are obtained as follows

$$r = \begin{cases} R/12.92, & R \leq 0.0405, \\ (\frac{R+0.055}{1.055})^{2.4}, & R > 0.04045, \end{cases}$$

$$g = \begin{cases} G/12.92, & G \leq 0.0405, \\ (\frac{G+0.055}{1.055})^{2.4}, & G > 0.04045, \end{cases}$$

$$b = \begin{cases} B/12.92, & G \leq 0.0405, \\ (\frac{B+0.055}{1.055})^{2.4}, & B > 0.04045, \end{cases}$$

The CIE XYZ color transformation and the CIE Lab transformation are obtained as follows,

$$[XYZ] = [rgb]\,[M]\,,$$

If (x_r, y_r), (x_g, y_g), (x_b, y_b) represent the chromaticity coordinates and (X_W, Y_W, Z_W) be the coordinates of the white point of the RGB system. The following values are calculated as,

$$X_r = x_r/y_r,$$

$$Y_r = 1,$$

$$Z_r = (1 - x_r - y_r)/y_r,$$

$$X_g = x_g/y_g,$$

$$Y_g = 1,$$

$$Z_g = (1 - x_g - y_g)/y_g,$$

$$X_b = x_b/y_b,$$

$$Y_b = 1,$$

$$Z_b = (1 - x_b - y_b)/y_b,$$

$$[S_r S_g S_b] = [X_W Y_W Z_W] \begin{bmatrix} X_r & Y_r & Z_r \\ X_g & Y_g & Z_g \\ X_b & Y_b & Z_b \end{bmatrix}^{-1}$$

The transformation matrix M is calculated as,

$$M = \begin{bmatrix} S_r X_r & S_r Y_r & S_r Z_r \\ S_g X_g & S_g Y_g & S_g Z_g \\ S_b X_b & S_b Y_b & S_b Z_b \end{bmatrix}$$

The Lab components are computed as,

$$L = 116 f_y - 16,$$

$$a = 500(f_x - f_y),$$

$$b = 200(f_y - f_x),$$

where,

$$f_x = \begin{cases} \sqrt[3]{x_r}, & x_r > \epsilon, \\ \frac{\kappa x_r + 16}{116}, & x_r \leq \epsilon \end{cases},$$

$$f_y = \begin{cases} \sqrt[3]{y_r}, & y_r > \epsilon, \\ \frac{\kappa y_r + 16}{116}, & y_r \leq \epsilon \end{cases},$$

$$f_z = \begin{cases} \sqrt[3]{z_r}, & z_r > \epsilon, \\ \frac{\kappa z_r + 16}{116}, & z_r \leq \epsilon \end{cases},$$

$$x_r = \frac{\mathbf{X}}{\mathbf{X}_r}$$

$$y_r = \frac{\mathbf{Y}}{\mathbf{Y}_r}$$

$$y_r = \frac{\mathbf{Y}}{\mathbf{Y}_r}$$

$$\epsilon = \begin{cases} 0.008856, & \text{Actual CIE Standard} \\ \frac{216}{24389}, & \text{Intent of the CIE Standard} \end{cases}$$

$$\kappa = \begin{cases} 903.3, & \text{Actual CIE Standard} \\ \frac{24389}{27}, & \text{Intent of the CIE Standard} \end{cases}$$

The X_r, Y_r, Z_r are the reference of the white point in the CIE XYZ colorspace. In the calculations the actual CIE standard is for the ϵ and κ.

The HSV color model is derived as,

$$H = \begin{cases} undefined, & MAX = MIN, \\ 60° \frac{G-B}{MAX-MIN} + 0°, & MAX = R \text{ and } G \geq B, \\ 60° \frac{G-B}{MAX-MIN} + 360°, & MAX = R \text{ and } G < B, \\ 60° \frac{B-R}{MAX-MIN} + 120°, & MAX = G, \\ 60° \frac{R-G}{MAX-MIN} + 240°, & MAX = B. \end{cases}$$

$$S = \begin{cases} 0, & MAX = 0, \\ 1 - \frac{MIN}{MAX}, & otherwise. \end{cases}$$

$$V = MAX.$$

This results in a vector representation for each pixel in an image. That is each pixel is represented as an intensity vector $\mathbf{V}$, with each element of the vector representing the intensity of the pixel in each of the indexed components. For example in a colored RGB image, vector (r,g,b) represents the intensity at a pixel location from each of the indexed components red, green and blue. Grayscale intensity edge detection is extended to indexed images by measuring the distance between two vectored pixels. Distances can be measured using any of the distance metrics used to measure the distance between two vectors. For example euclidean and vector angle distance are two metrics used to measure the difference between two pixel vectors. Euclidean distance and vector angle distance for two vectors $\mathbf{U}$, $\mathbf{V}$, with $\mathbf{U} = (u_1, u_2, u_3)$ and $\mathbf{V} = (v_1, v_2, v_3)$ are defined as follows

$$EuclideanDistance = \|\mathbf{U} - \mathbf{V}\|$$

$$\cos\theta = \frac{\mathbf{U}^T\mathbf{V}}{\|\mathbf{U}\|\|\mathbf{V}\|}$$

$$\sin\theta = \left(1 - \frac{(\mathbf{U}^T\mathbf{V})^2}{\|\mathbf{U}\|\|\mathbf{V}\|}\right)^{\frac{1}{2}}$$

where, $\| \bullet \|$ is the L_2 norm of the vector.

Euclidean distance and sine angle measure the dissimilarity between two color vectors, where as cosine angle measures the similarity between two color vectors. Colors which vary in intensity are referred as co-linear and colors which vary in hue or saturation are usually separated by an angle. It is observed that vector angles capture small color differences better than euclidean distance [51]. Also the convention is to represent non edges with zero and cosine angle represents large angular differences with zero. On the other hand sine angle is convenient as it represents collinear edges with zero angle and larger angle have larger sine values [51]. An edge detector is then defined as the maximum of the 8 pixel color differences using one of the metrics discussed above. The edge is defined as,

$$edge = \max_{1=1..8} D(\mathbf{U}, \mathbf{V})$$

where D is the distance metric used to compute the pixel color differences. In order to detect the prominent edges or edges corresponding to color discontinuities in an image we perform thresholding operation on the edges detected. Thresholds in our experiments are determined empirically. Figure 3.6 shows examples of euclidean distance, sine angle distance on an RGB iris images and the results of thresholding edge outputs using each metric on the normalized examples shown for segmentation. The next section discusses the multiscale method for the detection of macro features.

3.5 Mutiscale detection of macro features

The main objective of multi-scale approach is to detect a set of local interest points from an image. These points are further used for the purpose of object recognition, tracking, and other image matching tasks. Some of the interest point detectors are Harris corner detector, Laplacian detector, and Difference of Gaussian (DoG) detector. The Harris corner detectors detect regions with large gradients in all directions at a pre-determined scale. In order to detect local keypoints in an image which are invariant to scale changes of the image, the approach is extended to scale space [52]. This approach relates to searching for stable features across all scales of an image, using a continuous function of scale known as scale space. Gaussian function is observed to be the best scale-space kernel [53]. A scale-space $L(x, y, \sigma)$ is obtained by convolving the image I(x,y) with

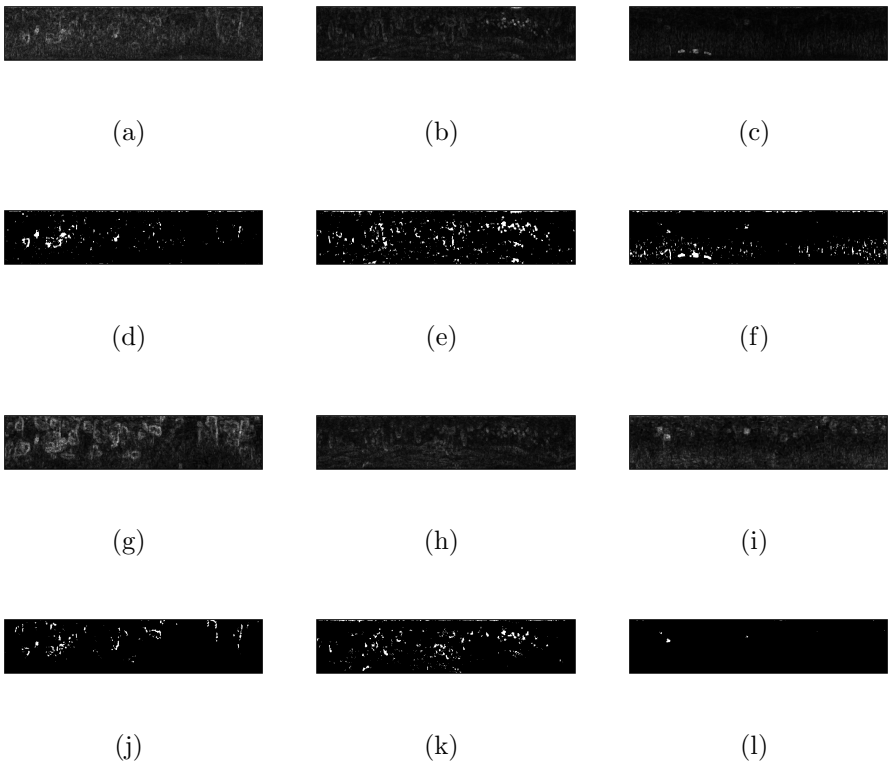

Figure 3.6: (a,b,c): Euclidean distance based edge detection, (d,e,f): Threshold operation on Euclidean distance, (g,h,i): Vector Sine angle distance based edge detection, (j,k,l): Threshold operation on Vector angle distance

a variable-scale Gaussian, $G(x, y, \sigma)$.

$$G(x, y, \sigma) = \frac{1}{2\pi\sigma^2} \exp^{-(x^2+y^2)/2\sigma^2}$$

The most stable features are detected by the Laplace of Gaussian (LoG), compared to all other detectors such as, gradient, Hessian and Harris corner detector [54]. The scale normalized Laplace of Gaussian is defined as $\sigma^2\nabla^2 G$, where G is the scale variable Gaussian kernel. The difference of Gaussians between two scales which are separated by a multiplicative factor k is defined as

$$D(x, y, \sigma) = G(x, y, k\sigma) - G(x, y, \sigma)$$

From the heat diffusion equation and finite difference approximation, the difference of

Gaussian can be approximated to scale normalized Laplace of Gaussians multiplied by a factor (k-1) [52], that is

$$G(x, y, k\sigma) - G(x, y, \sigma) \approx (k-1)\sigma^2\nabla^2 G$$

The difference of Gaussian scale space is defined as

$$DoG = (G(x, y, k\sigma) - G(x, y, \sigma)) * I(x, y) = L(x, y, k\sigma) - L(x, y, \sigma)$$

The above implementation is easier as it is computed as a difference of the Gaussian smoothed images.

The scale invariant feature transform based on DoG is used to detect regions with intensity discontinuities of different scales or sizes.

3.5.1 Scale invariant feature transform (SIFT)

The scale invariant feature transform detects local interest points which are invariant to scale and orientation. Which means that the points detected are stable at all scales and are not affected by the change in view angle which is angle in which the image is captured. The SIFT detections are obtained by first detecting the scale-space extrema detections at each scale and each location of the image, filtering the extrema detections based on stability, performing keypoint localization during which the location, scale of the interest point that is scale at which it is detected and the orientation of the keypoint is determined.

In order to detect the extrema points the initial image is incrementally convolved with Gaussians to produce images separated with a constant k in scale space. In each octave the difference of Gaussians are obtained by subtracting adjacent scales. Once an octave is processed the Gaussian smoothed image with scale twice the initial value of sigma is sampled by taking every second pixel in each row and column. Figure 3.7 shows the scale space at each octave on the left and the difference of Gaussians of the image on the right.

Local extrema points are determined by checking for maxima or minima at each location in the image. At each location a neighborhood defined as 8 neighbors in the current image and 9 neighbors each in the images above and below the current image in the Difference of Gaussian images is checked for extrema (maxima or minima) points. Figure 3.8

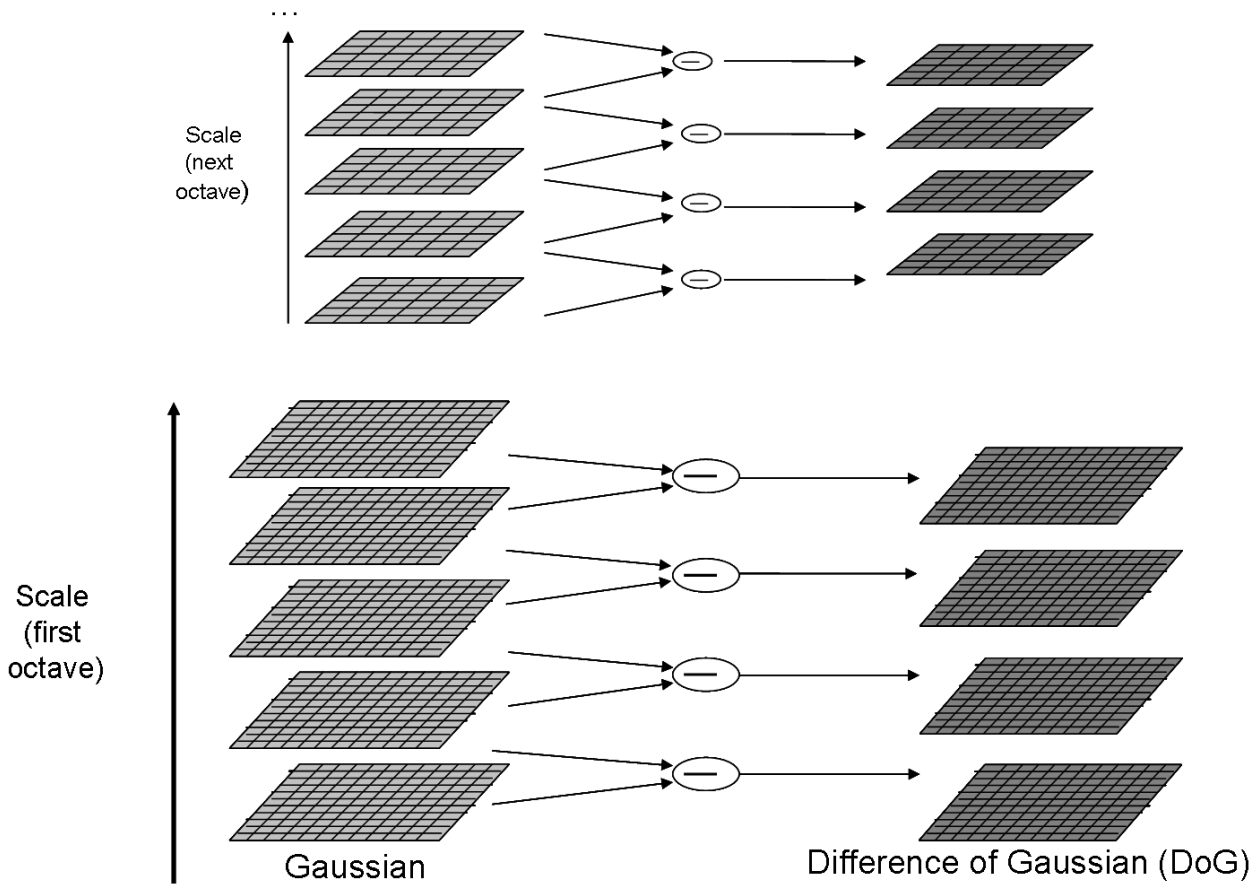

Figure 3.7: Left: Each octave of scale space is generated by repeated convolution of the initial image with Gaussians. The Gaussian image is down sampled and the process is repeated for the next octave. Right: Adjacent Gaussian smoothed images in each octave is subtracted to produce the Difference of Gaussian images

shows the neighborhood considered for each location. If a point is maximum or minimum in the neighborhood considered it is considered as a local extrema.

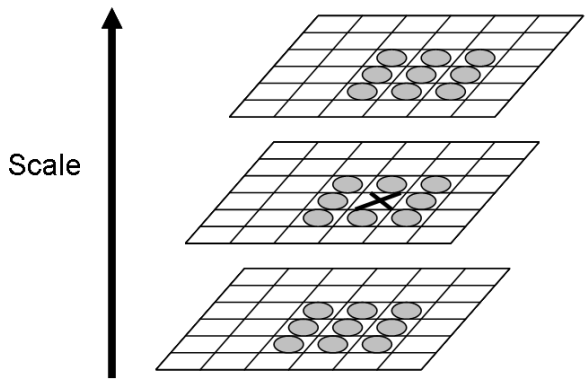

Figure 3.8: The pixel marked **X** is determined as an extrema point by comparing it with the 26 neighbors in the current DoG image and the DoG images above and below the current image

Once the local extrema are detected the next step filters the sample points based on the stability and fits the detected point to the near by data in order to compute the location and scale of the sample point. Many points may have low contrast and may be poorly localized along the edge. Such points are sensitive to noise and are filtered during this process. The extrema points are localized by fitting a 3D quadratic function to the local sample points to determine the interpolated location of the extrema points. This involves Taylor expansion of the scale space function $S = DoG(x, y, \sigma)$ upto quadratic terms, which are shifted so that the origin is at the sample point, that is,

$$S(\mathbf{x}) = S + \frac{\partial}{\partial \mathbf{x}}^T \mathbf{x} + \frac{1}{2}\mathbf{x}^T \frac{\partial^2 S}{\partial \mathbf{x}^2}\mathbf{x}$$

where, S and its derivatives are evaluated at the sample point with the offset from the sample point being $\mathbf{x} = (x, y, \sigma)^T$. The location of the extrema, $\widehat{\mathbf{x}}$ is obtained by taking the derivative of the function and setting it to zero,

$$\widehat{\mathbf{x}} = -\frac{\partial^2 D^{-1}}{\partial \mathbf{x}^2}\frac{\partial S}{\partial \mathbf{x}}$$

The Hessian and derivative of S are obtained from differences of neighboring sample

points. The resulting 3×3 linear system is solved and if the value of offset is greater than 0.5 in any dimension then the extremum is considered closer to a different sample point and the sample point is changed and interpolation is performed around the new point. The final offset $\widehat{\mathbf{x}}$ is added to the location of the sample point to get the location of the extremum.

The unstable extrema points with low contrast can be rejected by computing,

$$D(\widehat{\mathbf{x}}) = D + \frac{1}{2}\frac{\partial S^T}{\partial \mathbf{x}}\widehat{\mathbf{x}}$$

If $|D(\widehat{\mathbf{x}})|$ is less than 0.03 with the range of values of image pixels between [0,1], the extrema is rejected as low contrast point.

Another filtering process is to remove points with low principal curvatures. That is some extrema have strong response along the edge but are poorly localized and unstable to noise. A poorly defined peak in the difference of Gaussian has large principal curvature across the edge and a small principal curvature in the perpendicular direction. The principal curvatures are computed from the Hessian matrix computed at the location and scale of the keypoint by taking differences of neighboring sample points.

$$H = \begin{bmatrix} DoG_{xx} & DoG_{xy} \\ DoG_{xy} & DoG_{yy} \end{bmatrix}$$

The principal curvatures are proportional to the eigen values α and β, with $\alpha > \beta$. In order to discard keypoints with low principal curvatures in perpendicular direction to the edge, two conditions are checked,

1 If the curvatures have different signs.

2 If the ratio of principal curvatures is above a threshold r, where r is the ratio given by $\alpha = r\beta$.

These conditions are checked from the trace and determinant of the Hessian matrix. The trace $Tr(\mathbf{H})$ provides sum of eigen values and the determinant $Det(\mathbf{H})$ gives the product of the eigen values. If the determinant is negative it implies that the principal curvatures have opposite signs and the keypoint is discarded. The ratio between trace and determinant is proportional to the ratio between the principal curvatures as,

$$\frac{Tr(\mathbf{H})^2}{Det(\mathbf{H})} = \frac{(\alpha+\beta)^2}{\alpha\beta} = \frac{(r+1)^2}{r}$$

The ratio of trace and determinant is miminum when the two eigenvalues are equal and increases with increasing r, that is increasing ratio between the curvatures. Therefore keypoints with the ratio of principal curvatures greater than a threshold are eliminated. The experiments in this thesis use r = 10 and eliminate all those keypoints whose ratio between trace and determinant of the Hessian matrix around the keypoint is greater than the threshold r.

Orientation assignment

Each keypoint is represented using the spatial coordinates, scale of the Gaussian kernel at which it was detected, and orientation of the keypoint. Orientation of the keypoint is to assign a consistent orientation to the local extrema detected. This allows obtaining a descriptor at the extrema detected (discussed in 3.7.1), relative to the orientation assigned and results in a descriptor invariant to orientation. At this point, it is required to understand orientation assignment to understand why multiple SIFT keypoints are generated for a single object at the same location.

Using the scale of the keypoint we obtain the Gaussian smoothed image L. This allows computations which are scale invariant. From the Gaussian smoothed image the gradient magnitude m(x,y) and orientation $\theta(x, y)$ are computed at each location of the image. The gradient magnitude and the orientations are computed using the pixel differences in grayscale images as follows,

$$m(x,y) = \sqrt{(L(x+1,y) - L(x-1,y))^2 + (L(x,y+1) - L(x,y-1))^2}$$

$$\theta(x,y) = \tan^{-1}((L(x,y+1) - L(x,y-1))/(L(x+1,y) - L(x-1,y)))$$

An orientation histogram is computed around each keypoint detected with 36 bins covering the range of 360 degrees for orientation. The samples within a region around the keypoint are weighted by the gradient magnitude and a Gaussian - weighted circular window with standard deviation equal to 1.5 times the scale of the keypoint or the scale at which the keypoint is detected. This is done as the characteristic scale of the object

detected is approximated to a circle with radius $R = \sqrt{s}\sigma_{keypoint}$, where $\sigma_{keypoint}$ is the Gaussian scale at which the keypoint is detected [55]. The highest peak in the histogram is typically the orientation assigned to the keypoint. In some cases any other histogram peak which is within 80% of the highest peak is used to generate a new keypoint at the same location, with same scale and different orientation. For each of the peaks obtained a parabola is fit to the 3 histogram values closest to the peak. This is done to best interpolate the peak position or the orientation.

3.5.2 Database

The database used for the experiments is from the miles research. It is captured using the coaxial biometric illuminator. This equipment produces images with uniform illumination. The images are multispectral, high resolution color images in the standard RGB domain captured using the Nikon digital SLR. Miles database used for experiments consisted of 390 iris images with blue, hazel and brown iris with 1187 macro features in total which have been marked manually. Figure 3.9 shows the distribution of macro features across the database. The database is pre sorted from blue to brown irises. The distribution shows that the brown irises have fewer macro features compared to blue and green irises.

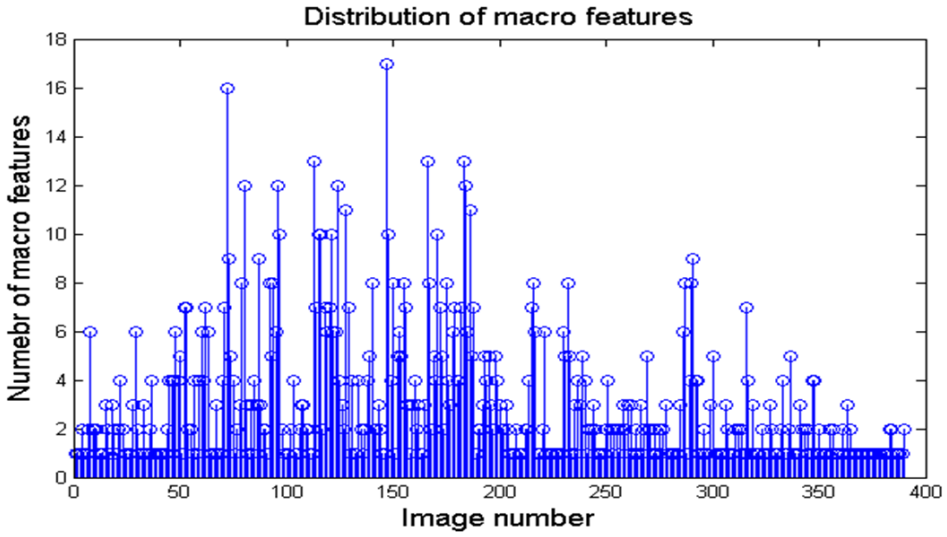

Figure 3.9: Distribution of macro features.

3.6 Experiment

The iris images in the database are preprocessed such that the iris-sclera boundary and iris-pupil boundary are localized manually and the iris is normalized using the Daugman's rubber sheet model. The macro features are detected on the normalized iris using region based and multi-scale based approach. The accuracy of detection is evaluated using the following experimental setups.

3.6.1 Experiment 1

Following is a brief description of the region based approach for the detection of macro features.

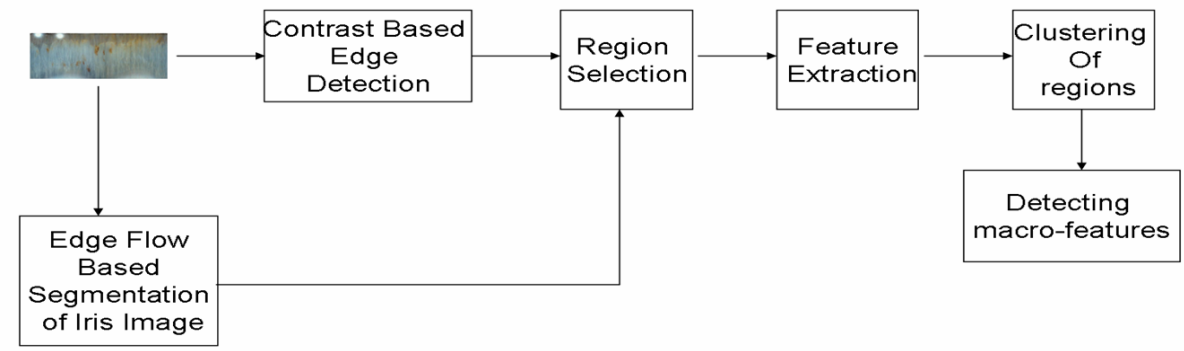

Figure 3.10: Block diagram of Region based detection of macro-features

The normalized iris is converted to Lab colorspace and subjected to edge flow based segmentation. Color edge detection is performed on the RGB colorspace using the vector angle distance. The edges detected in the previous step correspond to both macro features and non-macro features. The edges corresponding to non-macro features are detected due to the limitation that the edge magnitude changes with the change in the color of iris, change in the color of the macro features and the richness of iris texture specially in blue colored iris requiring a change in threshold for edge detection. Thus further pruning of the edges obtained as a result of edge detection is required. For further pruning feature extraction is performed in regions encompassed by the edges detected. This is

performed in order to obtain features corresponding only to the regions corresponding to the edges. The regions corresponding to the edges detected by color edge detection are selected either by region growing or defining a fixed size of region at each of the edge pixels resulting as an output of edge detection. Due to the variable size of the macro features it is inappropriate to define a fixed size region around the edges corresponding to a macro feature. Apart from this it is computationally expensive to perform region growing around spurious edge detections. We choose to perform region selection by fusing the results of image segmentation and edge detection. That is for each pixel obtained as a result of edge detection, its corresponding segmented region is obtained from the indexed segmentation map obtained as an output of edgeflow based segmentation. The features are extracted from regions selected as a result of vector angle based edge detection on RGB images. Figure 3.11 shows the result of performing region selection on edges detected using euclidean and vector angle metric on RGB image for the example irises shown in figure 3.4. A feature vector with the mean red, green, blue, hue and saturation is constructed for each of the regions selected. The feature vectors are classified to 3 clusters using the K-means algorithm. The cluster with the maximum macro features is selected manually and the algorithm is evaluated to check the number of macro features detected in the final cluster. The final evaluation is performed by evaluating the total number of macro features present in the final cluster selected for each image.

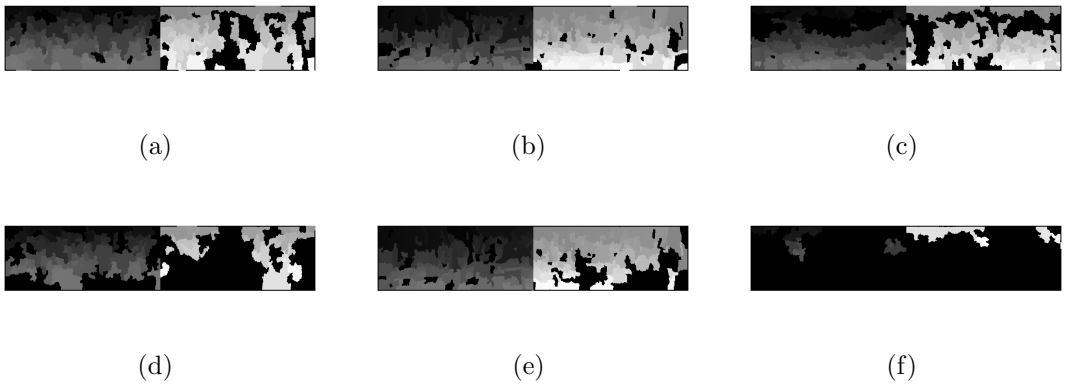

Figure 3.11: (a,b,c): Result of region selection on edges detected using euclidean distance, (d,e,f): Result of region selection on edges detected using Vector angle distance

The edge detection was performed both on the RGB and LAB colorspaces using both vector angle and euclidean distance. The thresholds were determined empirically. The

vector angle distance on RGB colorspace resulted in comparatively lesser regions selected and higher macro features selection. Figure 3.12 shows the results of region selection of edge detection on RGB colorspace using the vector angle for each image in the database. Table 3.4 shows the percentage area of mask, and the detection rate of macro features for combination of distance metrics Vector angle (VA), Euclidean (ED) and colorspaces RGB, Lab. The percentage area of mask is the ratio of total pixels retained from all the iris images in the database and the total size of all irises, in pixels in the database. The plot depicts that a large area is retained for certain irises during edge detection, which in our database are brown colored irises. The result of classification is shown in the Table 3.5. The true detection corresponds to percentage of macro features detected across all 390 images and false detections correspond to percentage of detected regions not corresponding to macro features.

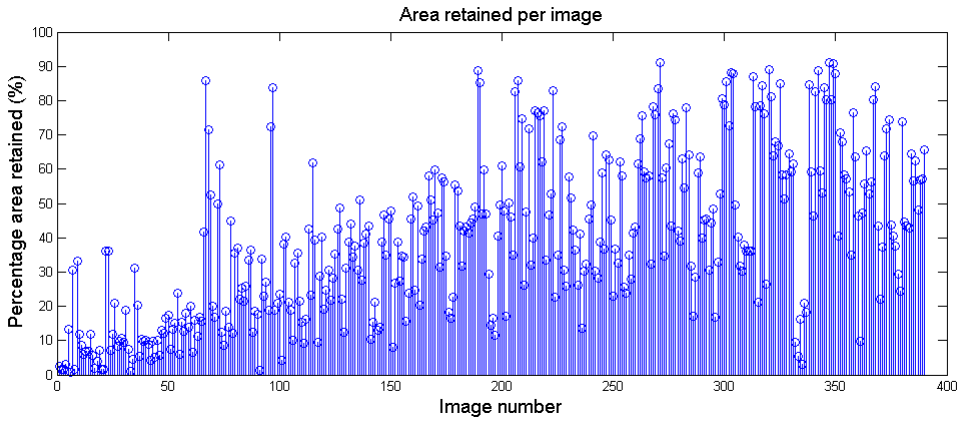

Figure 3.12: Plot depicting the percentage area retained per image as a result of region selection

Table 3.4: Evaluation of distance metric on each colorspace

metric_colorspace	Percentage area of mask	Detection rate of macro features
VA_RGB	39.05	90.83
VA_Lab	35.39	88.43
ED_RGB	77.57	96.2
ED_Lab	52.06	94.38

Table 3.5: Results for Region Based Approach

Ground Truth : Total number of manually marked features	1187
Total number of regions selected across 390 images before clustering	41353
Total number of regions selected across 390 images after clustering	16022
Percentage of true detection	864/1187, 72.78%
Percentage of false detection	15158/16022, 94.6%

3.6.2 Experiment 2

The scale invariant feature transform is applied to normalized iris from miles database, to detect the scale and rotation invariant local features. The SIFT is applied to red, green or blue component of the iris based on the color of the iris. The selection of the color component for each iris is done manually. This resulted in increase in detection rate of macro features compared to direct detection on grayscale converted images. The features at each keypoint are extracted to obtain a feature vector for classification. The features extracted are mean red, green, blue, hue and saturation in a window of size $2*1.5*\sigma$ at each of the local keypoints, where $1.5*\sigma$ is the radius of the circle that fits the object [55]. The local keypoint detections in image are classified using the K-means to 3 clusters and the cluster with the maximum keypoints matching the macro features is retained manually. Figure 3.13 is the block diagram of the algorithm to detect macro features at multiscale using SIFT.

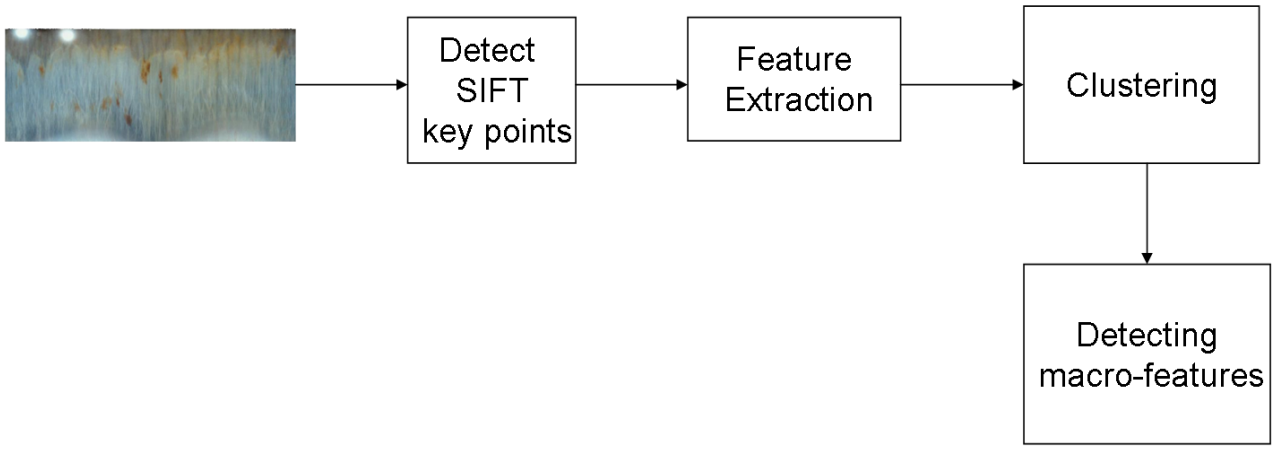

Figure 3.13: Block diagram of scale invariant based detection of macro features

Figure 3.14 shows the result of SIFT detections on the respective color channels for each of the examples shown for region based approach.

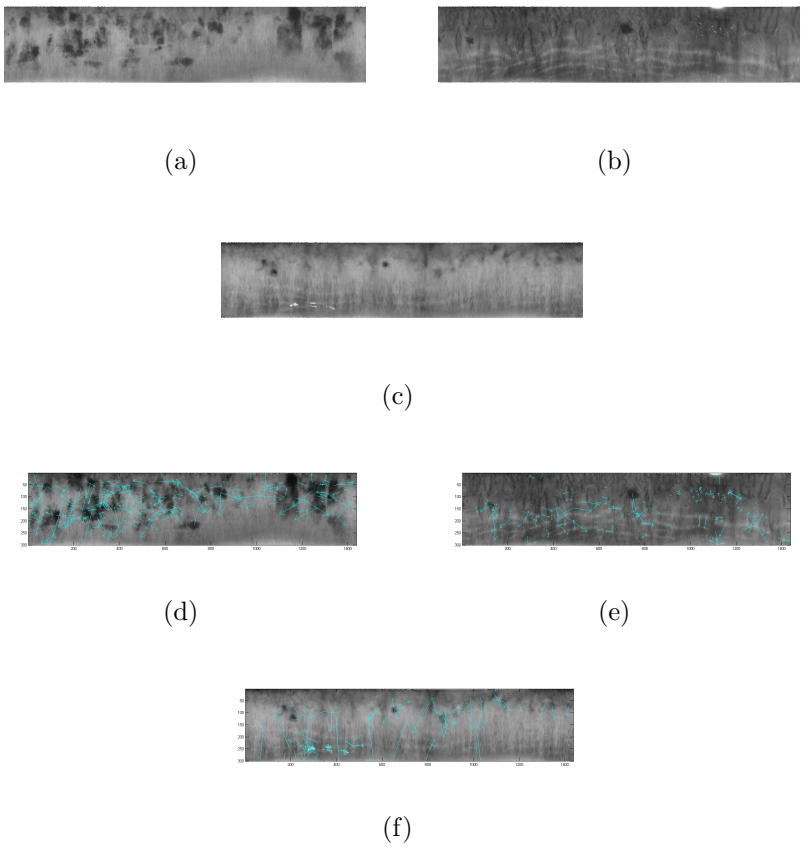

Figure 3.14: (a,b,c): Respective color channel for each iris example, (d,e,f): SIFT detections on the respective color channel

The result of the following experiment are as shown in Table 3.6. True detections correspond to percentage of macro features detected across 390 images. False detections are the percentage of SIFT detections not corresponding to macro features.

3.6.3 Summary on experiment 1

The region based approach has issues such as

- The number of regions selected as a result of edge detection and segmentation is about ≈ 33 times more than the number of regions representing the macro features.

Table 3.6: Results of multiscale detection of macro features

Ground Truth : Total number of manually marked features	1187
Total number of regions selected across 390 images before clustering	58333
Total number of regions selected across 390 images after clustering	22911
Percentage of true detection	1086/1187, 86.43%
Percentage of false detection	20227/22911, 88.28%

- The segmentation algorithm does not localize around macro-features of different sizes. That is, the segmentation algorithm does not localize on small macro features resulting in a region selection consisting of iris texture for the respective macro feature under consideration.

- The segmentation algorithm also fails in cases of macro features that are greater than thousands of pixels. In such cases the segmentation algorithm oversegments the macro features. This results in selection of regions only around the boundaries not encompassing the centroid of macro feature, which is a failure to detect the macro feature during the evaluation stage.

- The edges corresponding to macro features vary in intensity. A consequence of this is that weak edges are obtained. Reducing the threshold to increase the macro feature detection even for weak edges results in many spurious edges as a consequence of which a number of regions are selected from the segmentation map.

- The clustering still retains regions corresponding to spurious detections.

3.6.4 Summary on experiment 2

To overcome some of these issues such as, localizing the area of macro features which are too small in scale and to prevent the oversegmentation of macro features which are big in scale we choose the multiscale detection of macro features.

The SIFT detection resulted in a large number of keypoint detections due to the highly textrous iris. That is iris has many repeating textures at different scales such as crypts and many other textural features such as Wolfflin nodules and radial furrows, resulting in a large number of keypoint detections. It is observed that the keypoint detections are so large that the keypoints associated with 1187 macro features in our experiments correspond to only ≈ 3000 and the total number of SIFT detection is around ≈ 58000.

This resulted in further complexity to classify keypoints associated with macro features and false detections. Apart from this though the points are well localized in spatial and frequency domain the location of the keypoint is not always at the center of the object. Also due to the variable shape of the macro feature defining a window based on scale of macro feature resulted in feature extraction from the background iris texture. Apart from the issues of characterizing a macro feature, in some cases the macro features were very thin or elongated and small in size. In such cases SIFT failed to detect the macro feature.

The above results show that though the detection rate of macro features increased using multiscale approach, due to the highly textrous nature of iris and the variability in the nature of macro features it is difficult to detect discontinuities corresponding only to the macro features, and also that the macro features are similar in color and texture to other discontinuities within the same iris the problem of classification gets even more difficult.

Few other experiments were performed to reduce the number of keypoint detections or the regions selected from edge flow based segmentation for the purpose of classification. Figure 3.16, 3.17 show the block diagrams for the experiments. In the first experiment regions corresponding to the keypoint detections were selected from the indexed segmentation map obtained using edge flow based segmentation and along with the region corresponding to the keypoint, the surrounding regions are also selected from the indexed segmentation map. The indexed region on which the keypoint lies is the region corresponding to the keypoint. Figure 3.15 shows the region selection method for the SIFT keypoint detections.

The ratio of between class variance and within class variance is computed for the regions selected. The between class variance is computed between all the pixels surrounding the region selected and the pixels belonging to the keypoint region. Within class variance is the variance of pixel intensities in the keypoint region selected. The higher the ratio implies the higher image discontinuity in intensity. The threshold on this ratio was empirically determined in order to eliminate those SIFT detection which did not show considerable variation between classes. The ratio of between class variance and within class variance is computed as,

$$J = \frac{VAR_{BW}}{VAR_W}$$

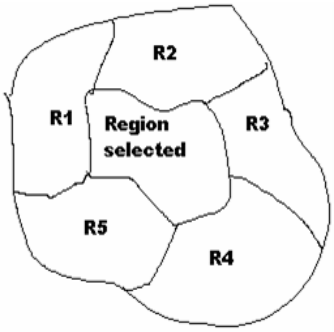

Figure 3.15: Regions surrounding the region selected for a keypoint. R1, R2,R3, R4, R5 are the surrounding regions encompassing the region selected for a keypoint

where VAR_{BW} denotes between class variance and VAR_W denotes within class variance. The above experiment was performed to reduce the total number of SIFT detections for the purpose of further processing.

In another experiment the above two algorithms were used parallely. That is the iris images were segmented and the regions were selected for the edges obtained as a result of edge detection. The SIFT detections are performed on the normalized iris images. The regions are then selected for the SIFT detections which lie on the final regions grown as a consequence of edge based detection. Ideally, a parallel configuration could reduce either the SIFT detections or the number of regions selected by SIFT for the purpose of classification.

These experiments however resulted in lesser detection rate for macro features and the issue of many keypoint detections or regions considered for the purpose of classification persisted. The result of combining the two methods is shown is Table 3.7.

Table 3.7: Results of classification of SIFT keypoints detected after edge detection,region selection for SIFT keypoints detected

Number of marked macro features	1187
SIFT detections retained after classification	11930
Macro features retained	945/1187, 79.6%
SIFT keypoints corresponding to macro features	2478

The focus of this thesis was to detect macro features for the purpose of proposing a new set of points to perform iris recognition and image retrieval. We had proposed to detect

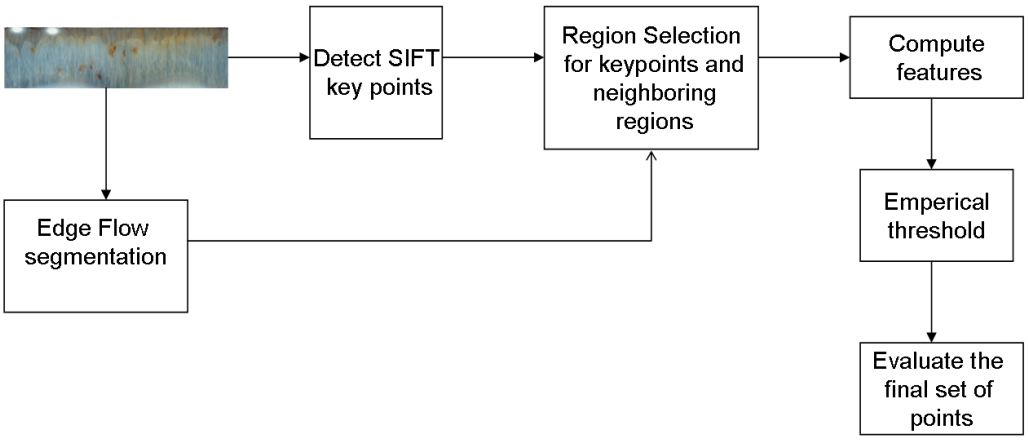

Figure 3.16: Block diagram for combination of edge flow based segmentation and SIFT detections of macro features

certain macro features in two irises and determine a match result by matching these macro features between the two irises. As seen from the experiments it is a difficult problem to detect only the macro features. A large number of spurious discontinuities are detected. These discontinuities can be used for the purpose of matching two irises. [30, 32, 56] have extended iris recognition using local keypoints. We propose to perform partial iris recognition using the keypoints detected. That is, to match a partial iris with the whole iris based on features extracted around the keypoints detected. In some cases these keypoints correspond to extended set of macro features which would be other anatomical structures present in the iris as discussed in Chapter 1. Furthermore the ability of macro feature to perform macro feature recognition and help in image retrieval by identifying the iris containing the query macro feature is also examined.

3.7 Partial Iris recognition using local keypoints detected

Partial irises occur as a result of occlusions due to eyelids and eyelashes, pupil dilations and off-angled irises. Figure 3.18 shows examples of partial irises and Figure 3.19 shows

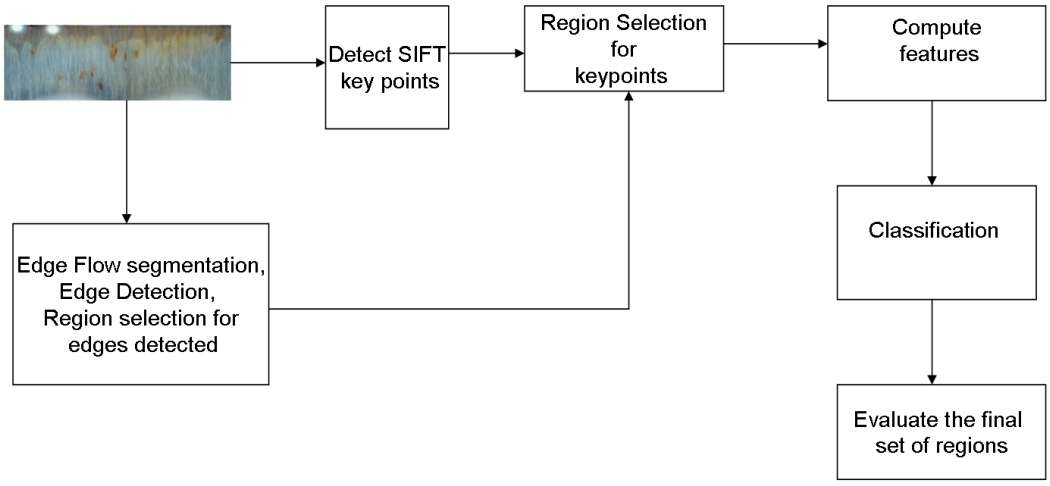

Figure 3.17: Block diagram for combination of edge detection, region selection and SIFT detections of macro features

the block diagram for the recognition of iris using sift descriptors.

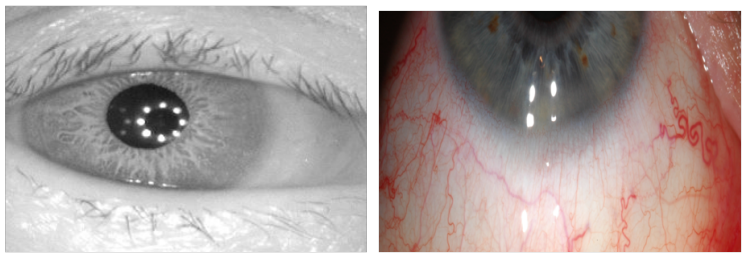

(a) (b)

Figure 3.18: (a): Partial iris due to eyelid occlusion, (b): Partial iris due to off-angled iris

As discussed in the previous sections the SIFT is applied to the normalized or enhanced iris texture. As a result of execution of SIFT on an iris image, a large number of keypoint detections are obtained, which can be used for partial iris recognition. These keypoints are used for recognition using SIFT descriptors as discussed in the next section.

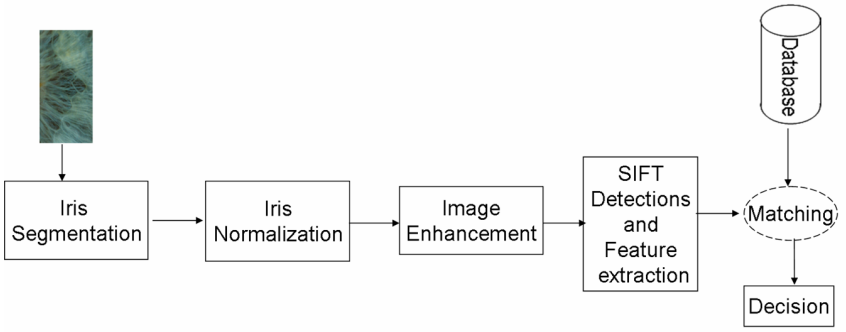

Figure 3.19: Block diagram to perform partial iris recognition using keypoints detected

3.7.1 SIFT Descriptors

As discussed earlier the SIFT descriptors are computed relative to the orientation assigned to the keypoint. This results in a descriptor which is invariant to rotation. Like in the case of orientation assignment the Gaussian blurred image L is obtained from the scale of the keypoint. The gradient magnitude and orientation are computed at each location of the image. The gradient magnitude and orientations are sampled from a descriptor region of size 16 X 16 window around the keypoint. The sampled gradient orientations and coordinates of the descriptor are rotated relative to the orientation of the keypoint. This provides orientation invariance or rotation invariance [52]. Each of the sample points magnitudes in the descriptor window are weighted using a Gaussian weighted function with σ equal to half the width of the descriptor window. The keypoint descriptor is computed as a 8 bin orientation histogram over 4 X 4 sample regions within the descriptor window. In order to mitigate the effects of a sample point shifting from one histogram to other, tri-linear interpolation is used to distribute the value of each gradient sample to adjacent histogram bins. Each entry to a bin is multiplied with a weight 1 - d for each dimension, where d is the distance of the sample from the central value of the bin as measured in units of the histogram bin spacing. This results in a descriptor of size 4 X 4 X 8 = 128 dimensions. The descriptor is then normalized to unit length to reduce the effects of illumination changes such as affine illumination changes. Further processing is done to reduce the effects of nonlinear illumination changes [52]. Figure 3.20 shows the image gradients and keypoint descriptors around a keypoint using a descriptor window of size 8 X 8, and 2 X 2 sample regions each of size 4 X 4.

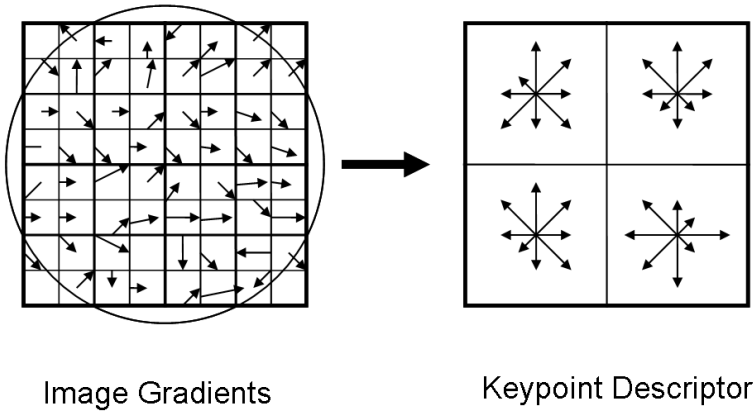

Figure 3.20: Example of descriptor computation on an 8 X 8 region around the keypoint

3.7.2 Matching

The output of the matching algorithm is the number of keypoint correspondences obtained. In order to obtain the number of correspondences the SIFT detections from two images are matched using the descriptors extracted for each keypoint detected. The descriptors are matched using the nearest neighbor matching, according to which a matching correspondence is the keypoint from the set of keypoints which has the minimum distance between the query keypoint and all other keypoints of the image in the database. In order to obtain reliable matching and prevent discarding possible matches using global threshold the top two closest matches are compared. This results in correct closest match which is significantly closer than the second closest incorrect match. The cosine similarity metric is used to obtain the similarity measure between two keypoint descriptors $\mathbf{des}_1$ and $\mathbf{des}_2$. The cosine angle is defined as,

$$Theta = \cos^{-1}\left(\frac{\mathbf{des}_1^T \mathbf{des}_2}{\|\mathbf{des}_1\|\|\mathbf{des}_2\|}\right)$$

The closest correct match is obtained with high probability if the first closest match is lesser than 0.6 times the second closest match.

3.7.3 Experiment

Matching experiments were performed on the UPOL database. Experiment performs iris recognition using partial iris images and the whole iris. The segmented iris images are normalized and enhanced using the CLAHE as described in Chapter 2. SIFT keypoints are detected for the partial probe images and are compared against the SIFT detections for each image in the database. Experiments consist of performing SIFT detections on 10, 30, 50 and 75 percent of the probe iris and matching with the SIFT detections on the 100% of each iris in the database. Figure 3.21 shows the partial irises and the matching result of 30% iris with the 100% iris. Figure 3.22 shows the ROC plots for each of the keypoint matching experiment on the UPOL database. The number of correspondences are normalized between 0 and 1 in each of the experiments. It consisted of 384 genuine and 73152 impostor scores from total of 64 subjects each with 3 left and right iris images.

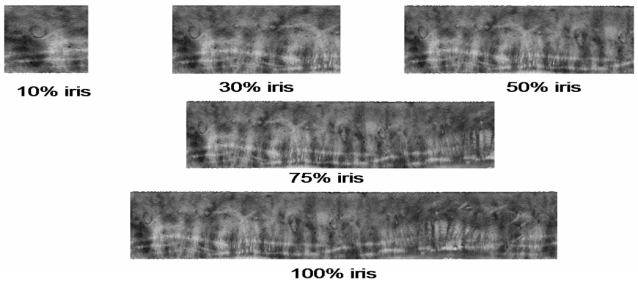

(a) Partial irises

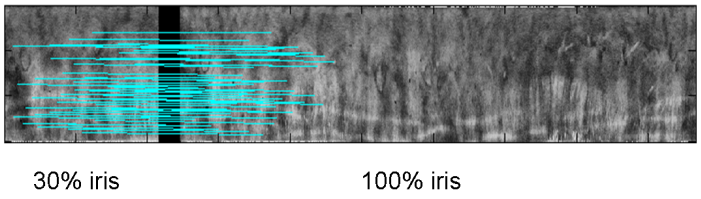

(b) Partial iris matching

Figure 3.21: Partial iris images representing 10, 30, 50, 75 and 100 percent of the normalized iris. 3.21(b) result SIFT matching between 30% and 100% irises using keypoint descriptors

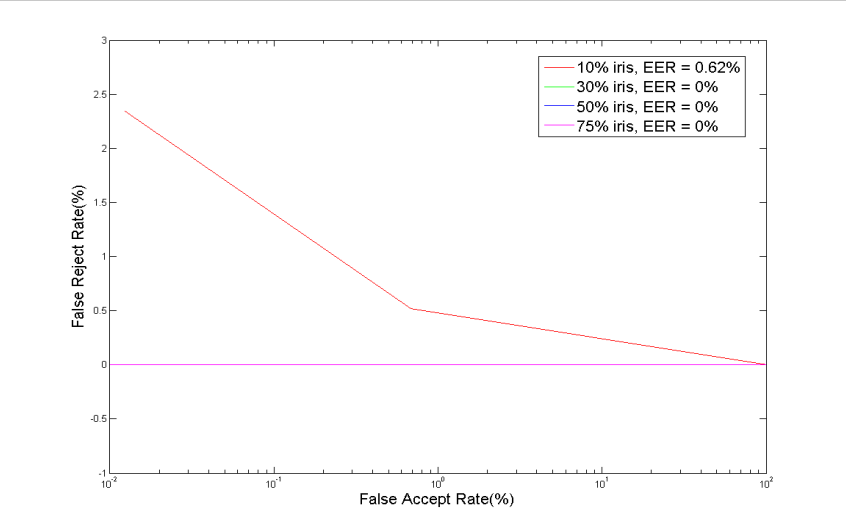

Figure 3.22: ROC plots for matching partial iris

3.7.4 Analysis

It is observed that with the increasing percentage of the iris the equal error rate decreases. In fact it shows recognition using just 30% of the iris results in an equal error rate of zero percent. One reason for high error rate matching 10% of iris could be the fact that we do not look for correspondences based on locations of keypoints. That is for example if we extract the 10% of iris from the left most of the normalized iris region, it should not be matched to features from the right most portion of the normalized iris. This could be the reason for high error rate, as SIFT detects local features in iris at different scales and we perform matching only based on descriptors and not on the relevance to region. As seen in [32], Belcher and Yingzi performed region based relevance experiments and got low equal error rates of 5.57% and 8.28% on ICE and WVU database.

3.8 Summary

It is observed that with the increasing percentage of the iris and with the region relevance the performance can be increased. Apart from this the local keypoints detected by SIFT on the UPOL database corresponded to image discontinuities induced due to enhancement operation. Figure 3.23 shows the UPOL images before and after enhancement

and the SIFT detections on the images before and after enhancement. But in the experiments for detection of macro features due to the resolution and the coaxial illumination used to capture the database there was no requirement to perform enhancement on the images. On observation, we find that the SIFT keypoint in the case of miles database corresponds to the iris characteristics such as the macro features, Lisch nodules, Wolfflin and Brushfields spots, anterior layer exposed due to crypts and the fibrous texture. These may be considered as extended macro features. Figure 3.24 shows the results of SIFT detections on the segmented miles iris database. Based on the results of UPOL, the perfomance can be improved with regional relevance and using local keypoints corresponding to extended macro features. Figure 3.25 shows the results of SIFT matching on samples of the same eye of the subject, matching of left and right eyes of subject, matching the original and rotated samples of the subject. This shows that these features can be used reliably with the region relevance for recognition.

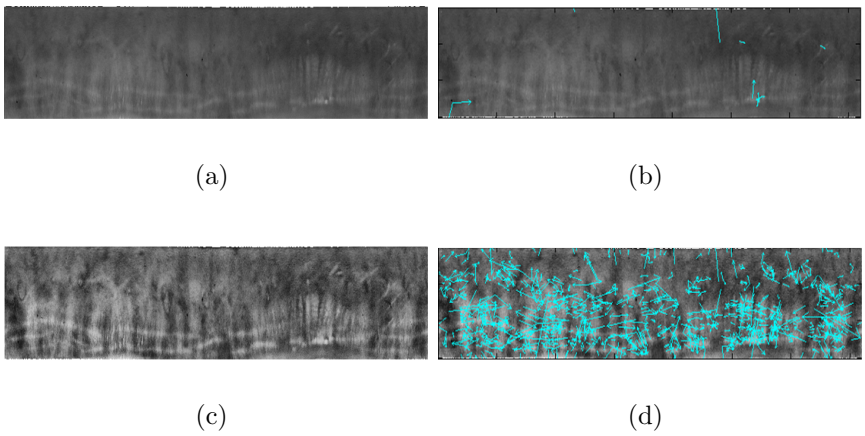

(a) (b)

(c) (d)

Figure 3.23: Results of SIFT detections on the UPOL database. Above: Original and enhanced iris images. Below: SIFT detections on the original and enhanced iris images

Based on the observation of SIFT detections on the macro features and other iris structures the reliability of these extended macro features to perform iris recognition can be explored as shown in Figure 3.25. These macro features may also be used for the purpose of image retrieval. A simple experiment is performed using the macro features for the purpose of image retrieval or identity retrieval as discussed in the following section.

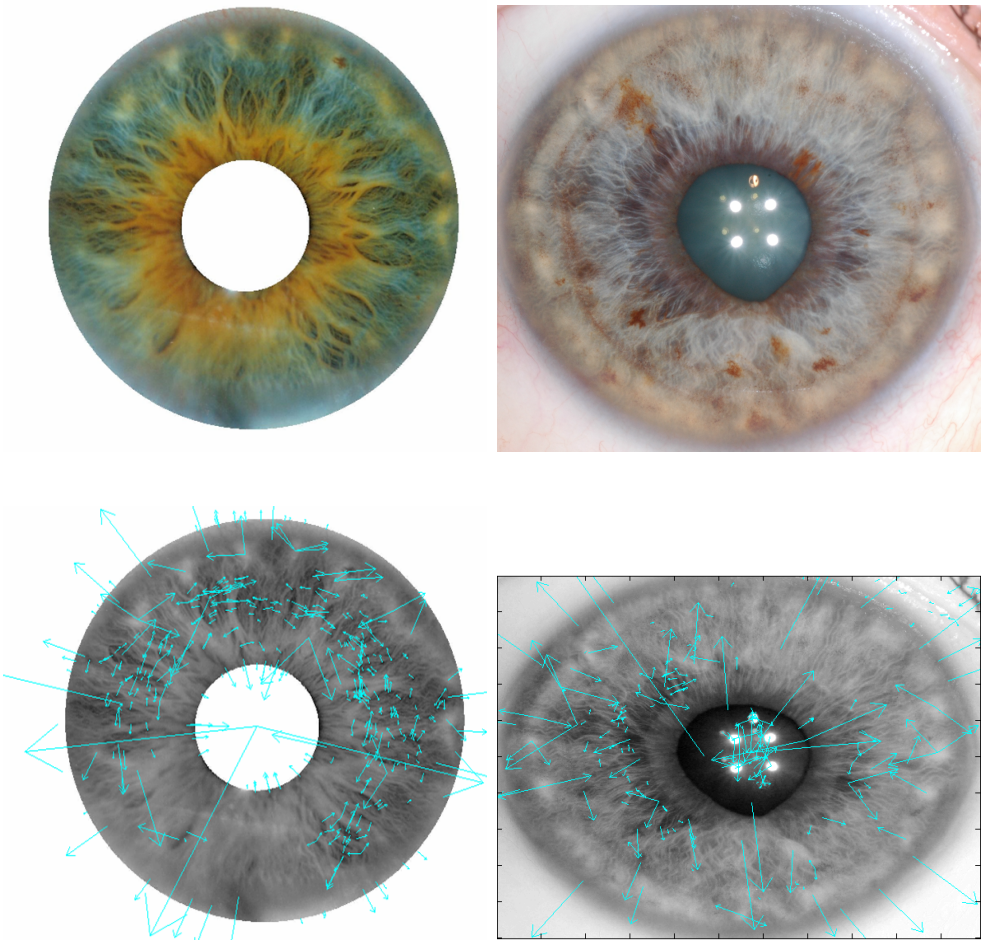

Figure 3.24: Above: Example of iris images from miles database. Below: SIFT detection on miles database showing the detections of iris characteristics such as crypts and white spots.

3.9 Macro feature recognition and image retrieval

From the example images in Figure 3.25 there seemed a potential for iris recognition using these macro features. The successful recognition of these macro features will result in,

1. Image retrieval by matching the macro features and
2. Establishment of new set of minutiae points which can be used for the purpose of recognition of two iris images.

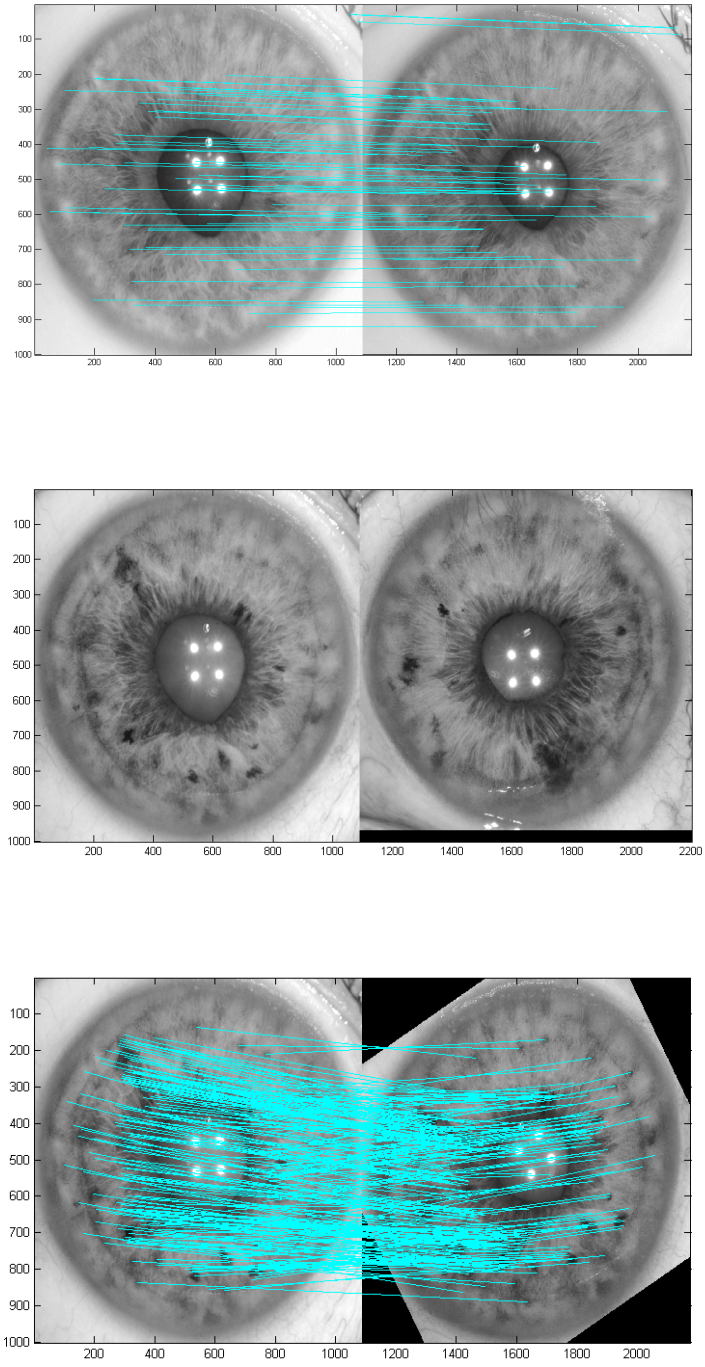

Figure 3.25: Results of SIFT matching on samples of two left eyes, samples of left and right eye, samples of left and sample rotated by 30 degrees

A simple experiment is performed to determine, if the macro features can indeed retrieve images from the database and be used as a new characteristic in addition to traditional features used for iris recognition.

3.10 Database

As mentioned earlier the miles database with the marked macro features is used for the experiments. The database of macro features consists of 1187 macro features and the gallery of iris images consists of 390 iris images from which the macro features are extracted and 380 iris images without any iris characteristic. In image retrieval experiment a set of 500 randomly selected macro features are used. Figure 3.26 shows examples of the macro features used in the experiments.

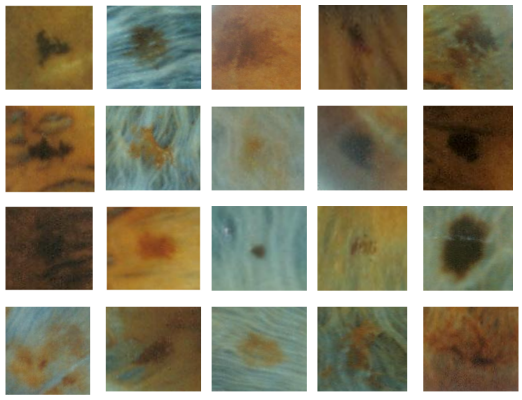

Figure 3.26: Examples of macro features in the database.

3.11 Experiment

Figure 3.27 shows the block diagram for image retrieval experiment. Based on the color of the iris the red, green or blue component is used for the purpose of the experiments both for the query macro feature and the gallery iris image. The query macro feature is subjected to SIFT keypoint detection and characterized using the SIFT descriptors. The set of query keypoints Q_k are matched to each of the gallery iris's keypoints G_k and the

top K identities are retrieved based on the closest match of the query keypoints to the gallery iris image's keypoints. The closest match is determined by the number of keypoint correspondences obtained between Q_k and G_k. The top k identities are retrieved based on the maximum number of keypoint correspondences obtained.

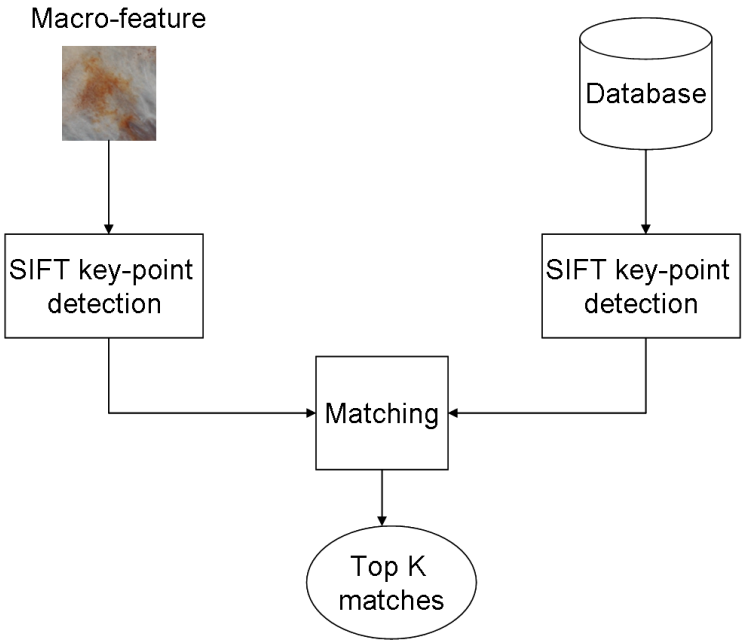

Figure 3.27: Block Diagram for image retrieval using macro-features

3.12 Results

Figure 3.28 shows the examples of query macro feature and the 3 false identities with same match score retrieved as a result of matching at rank 1 which is due to detection of just one keypoint associated with the macro feature. The graph in Figure 3.29 shows the cumulative curve for the image retrieval experiment where, a hit is the case when the iris image from which the macro feature is extracted is retrieved among the top k images. We observe a hitrate of 88.2% at rank 2.

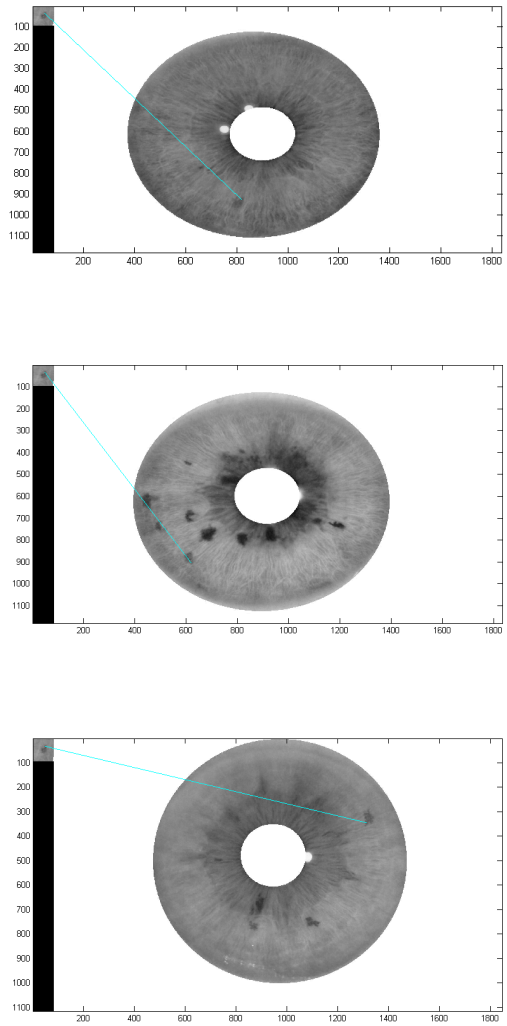

Figure 3.28: Examples of false identities retrieved as a result of image retrieval using macro features

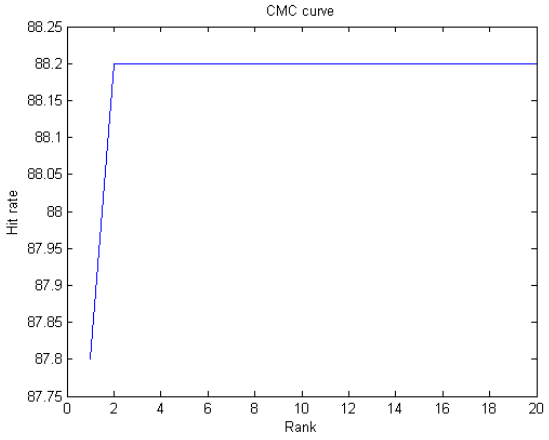

Figure 3.29: Cumulative match characteristic curve for image retrieval using macro features

3.13 Summary and Future work

The above experiment shows that a hitrate of 88.2% is obtained at rank 2. Which means that the identity from which the macro feature is extracted is among the top two identities retrieved. This shows the potential of macro features to be used as additional set of features for the purpose of iris recognition and image retrieval. A higher hitrate could not be obtained due to algorithmic issues such as a homogeneous macro feature is characterized only by one keypoint and in some cases by zero keypoints.

This work can further be extended and explored to perform iris recognition for images with macro features using SIFT. Apart from this the features describing the macro feature may be improved. Additional information such as location and other textural characteristics describing a macro feature may be incorporated in the experiment for image retrieval. Furthermore the experiments are performed by selecting a color channel based on the color of the iris. This process is done manually and may be automated.

Chapter 4

Conclusion and Future work

4.1 Conclusion

In this thesis it is observed that high classification accuracy is achieved using statistical features extracted from small blocks of iris. Also that smaller blocks provided higher classification than larger dimensioned blocks. Detection of macro features proposed in this thesis is a difficult problem. Though detection of macro features is a difficult problem the image retrieval experiment using macro features, the sample results for macro feature matching as shown in Figure 3.25 and results of partial iris matching using SIFT establish the potential of these macro features to be proposed as a new set of features in addition to the existing techniques. These macro features may serve as landmarks and aid iris recognition by matching landmarks and also aid in image retrieval.

4.2 Future Work

As seen in this thesis detection of these macro features with simple image processing technique would not be possible. The algorithm may need an in depth understanding of the characteristics of the macro features such as size, shape, categories of macro features, texture and color of both the iris and the change in color and texture based on the color and texture of iris. For example the detection techniques may be varied based on the color of the iris. Further it may be varied based on the texture of the iris. As seen from the [19] classification of iris, we see that within the blue iris there is a change in texture

due to which any edge detection technique would detect many edges. The problem would be to classify these edges from the edge corresponding to macro features. Apart from this the algorithm must take in to account the intensity variations of the macro features within the same iris and the changes in contrast in dark colored irises. Another aspect to be considered would be the type of macro feature. For example sectoral heterochromia may need different segmentation techniques as they correspond to a large iris region and usually end up in over-segmentation using the method of edge flow based segmentation described in Chapter 3.

Some of the other extensions which are possible would be,

1. The keypoints detected may be matched using other descriptors or other detectors may be used to detect stable keypoints. These keypoint can also be matched based on relevance such that the left portion of normalized iris is always matched with the left portion like in [32]. In addition to SIFT based recognition other patch based recognition techniques can be applied to improve the performance of image retrieval and recognition. This is useful in cases when the SIFT fails to detect keypoints around the macro feature for matching.

2. Potentiality of the macro feature to search the database and retrieve a small number of identities is already seen. This is achieved by performing object recognition in each of the images in the database. Image retrieval using multiple macro features from an iris image can be performed. It can also be improved by incorporating the information of each macro features position on the segmented iris defined by an angle between 0-360 degrees. Given a small patch of macro feature with the angular position, each image in the database can be searched. Figure 4.1 shows the object recognition applied directly on the image. The patch is obtained from one sample of the subject and the object recognition is performed on the other sample. Region relevance that is the coordinates of the patch are not used to limit the search in the sample iris. Advantage of SIFT based recognition is that it is rotation invariant and is not affected if the query macro feature is rotated or the gallery iris image.

3. Apart from this the keypoints detected may be used to perform indexing or classification of iris. Each of the keypoints detected on the iris in the database can be clustered to a pre-determined set of clusters. A frequency count of each of the

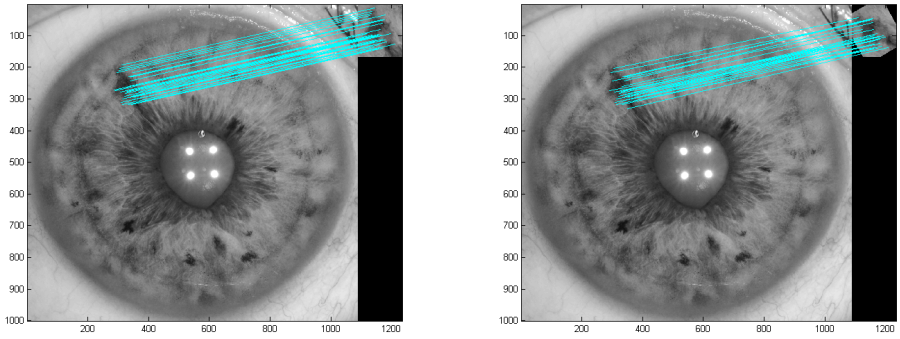

(a) (b)

Figure 4.1: (a) Object recoognition on the sample iris image, (b) Recognizing rotated object on the sample iris.

keypoint classes can be used to create a feature vector. This feature vector can be used to create a class of irises or used to create an index number. When a test image is presented the same process can be repeated and the features extracted may be used to determine the class of the iris or to retrieve identities which have similar index numbers generated based on the frequency counts.

References

[1] C. George, "Basic structure of the human eye," Disabled World, 6 2007.

[2] Jon Miles, *Miles Research*, `http://www.milesresearch.com/`.

[3] Adam, "Heterochromia," The New York Times, 2007.

[4] M Larsson and L. Nancy Pedersen, "Genetic correlations among texture characteristics in the human iris," *Molecular Vision*, vol. 10, pp. 821–831, 2004.

[5] Y Li, Z David, K Wang, and W Yang, "Coarse iris classification using box-counting to estimate fractal dimensions," *The Journal Pattern Recognition Society*, vol. 38, pp. 1791–1798, 2005.

[6] X Qiu, Z Sun, and T Tan, "Global texture analysis of iris images for ethnic classification," *Proceedings of International Conference on Biometrics, Lecture Notes in Computer Sciences*, vol. 3832, pp. 411 – 418, 2005.

[7] J Portilla and P. Eero Simoncelli, "A parametric texture model based on joint statistics of complex wavelet coefficients," *International Journal of Computer Vision*, vol. 40, no. 1, pp. 49–71, June 2000.

[8] A Muron and J Pospisil, "The human iris structure and its usages," *Physica*, vol. 39, pp. 87–95, March 2000.

[9] L. Flom and A. Safir, "Iris recognition system," .

[10] Daugman J, *Anatomy and Physiology of the Iris*, `http://www.cl.cam.ac.uk/~jgd1000/anatomy.html`.

[11] US National Institutes of Health, "Intraocular eye melanoma treatment," Tech. Rep., National Cancer Institute, `http://www.cancer.gov/cancertopics/pdq/treatment/intraocularmelanoma/HealthProfessional/page2/`, 2007.

[12] A. Tantri, WLM. Alward, and TA. Weingeist, "Iris melanoma: 47 yo man referred in 1997 for evaluation of iris lesion os," Tech. Rep., EyeRounds.org, February 2005.

[13] E Henderson and E. Curtis Margo, "Iris melanoma," *Archives of Pathology and Laboratory Medicine*, vol. 132, no. 2, pp. 268–272, February 2008.

[14] AD. Singh, L. Bergman, and S. Seregard, "Uveal melanoma: epidemiologic aspects," *Ophthalmology Clinics of North America*, vol. 18, no. 1, pp. 75–84, March 2005.

[15] A. David Lee and J. Eve Higginbotham, *Clinical Guide to Comprehensive Ophthalmology*, THIEME MEDICAL PUBLISHERS, 1 edition, 1999.

[16] E. Weis, CP. Shah, and jousm M.et.al La, "The association between host susceptibility factors and uveal melanoma: a meta-analysis," *Archives of ophthalmology*, vol. 124, no. 1, pp. 54–60, January 2006.

[17] Roberto R, Paulo S, Fabio D, Jaime R, and Rubens B Jr, "Iris recognition as a biometric method after cataract surgery," *BioMedical Engineering OnLine*, vol. 3, no. 1, January 2004.

[18] Wistrand PJ, Stjernschantz J, and Olsson K, "The incidence and time-course of latanoprost-induces iridial pigmentation as a function of eye color," *Survey of Ophthalmology*, vol. 41, no. 2, pp. 129–138, February 1997.

[19] M Larsson, *Human Iris Characterisitics as a Biomarker for Personality*, Doctorial, Orebro University, 2007.

[20] M Larsson, L. Nancy Pedersen, and H Stattin, "Importance of genetic effects for characteristics of the human iris," *Twin Research*, vol. 6, pp. 192–200, 2003.

[21] M Larsson, L. Nancy Pedersen, and Hakan S, "Associations between iris characteristics and personality in adulthood," *Biological Psychology*, 2007.

[22] L Masek, "Recognition of human iris patterns for biometric identification," M.S. thesis, University of Western Australia, 2003.

[23] Samir S, "Novel techniques for iris segmentation and sythesis," M.S. thesis, West Virginia University, 2006.

[24] J Daugman, "Probing the uniqueness and randomness of iriscodes: Results from 200 billion iris pair comparisons," *Proceedings of the IEEE*, vol. 94, no. 11, 2006.

[25] R. Wildes, J. Asmuth, G. Green, S. Hsu, R. Kolczynski, J. Matey, and S. Mcbride, "A system for automated iris recognition," in *Proceedings of the Second IEEE Workshop on Applications of Computer Vision*, 1994, pp. 121–128.

[26] W.W. Boles and B. Boashash, "A human identification technique using images of the iris and wavelet transform," *IEEE Transactions on Signal Processing*, vol. 46, no. 4, pp. 1185–1188, April 1998.

[27] K. Bae, S. Noh, and J. Kim, "Iris feature extraction using independent component analysis," in *Proceedings* 4^{th} *International Conference on Audio and Video Based Biometric Person Authentication (AVBPA)*, Guildford, UK, 2003, pp. 838–844.

[28] L Ma, T Tan, Y Wang, and D Zhang, "Efficient iris recognition by characterizing key local variations," *IEEE Transactions on Image Processing*, vol. 13, no. 6, June 2004.

[29] H Sung, J Lim, Ji-hyun Park, and L Yillbyung, "Iris recognition using collarette boundary localization," in *Proceedings of the 17th International conference on ICPR 2004*, August 2004, vol. 4 of *23-26*, pp. 857–860.

[30] W Yang, L Yu, L Guangming, and K Wang, "Iris recognition based on location of key points," in *Biometric Authentication*. July 2004, vol. 3072, Springer Berlin / Heidelberg.

[31] V. Conti, G. Milici, F. Sorbello, and S. Vitabile, "A novel iris recognition system based on micro-features," Automatic Identification Advanced Technologies,2007 IEEE Workshop on, June 2007.

[32] C Belcher and D Yingzi, "Region-based sift approach to iris recognition," *Optics and Lasers in Engineering*, vol. 47, pp. 139–147, 2009.

[33] J OBE Daugman and I Malhas, "Iris recognition border-crossing system in the uae," *Airport Review*, vol. 2, 2004.

[34] Rajiv M, "Indexing techniques for fingerprint and iris databases," M.S. thesis, West Virginia University, 2007.

[35] R. Mukherjee and A. Ross, "Indexing iris images," in *19th International Conference on Pattern Recognition, ICPR 2008.*, December 2008, pp. 1–4.

[36] Nirupam Sarkar and B. B. Chaudhuri, "An efficient differential box-counting approach to compute fractal dimension of image," *IEEE Transactions on System, Man and Cybernetics*, vol. 24, no. 1, pp. 115–120, January 1994.

[37] Sarvesh M, "Analyses and synthesis of iris images," M.S. thesis, West Virginia University, 2005.

[38] S. Makthal and A. Ross, "Synthesis of iris images using markov random fields," *Proc. 13th European Signal Processing Conf.*, 2005.

[39] G Lahouari, B Ahmed, and K. Ibrahim Mohammad, "Image compression using texture modelling," *IEEE International Symposium on Circuits and Systems*, vol. 3, pp. 2313 – 2316, May 2005.

[40] M. Tuceryan and K. Anil Jain, *"Texture Analysis", Handbook Pattern Recognition and Computer Vision*, chapter 2, pp. 235–276, World Scientific Publishing Co, 1993.

[41] D Kramer and F Aghdasi, "Texture analysis techniques for the classification of microcalcifications in digitised mammograms," *AFRICON, IEEE*, vol. 1, pp. 395–400, 28 Sept - 1 Oct 1999.

[42] M. Robert Haralick, Shanmugam K., and Its'Hak Dinstein, "Textural features for image classification," *IEEE Transactions on Systems, Man and Cybernetics*, vol. 3, no. 6, pp. 610–621, November 1973.

[43] K. S. Fu, *Syntactic Pattern Recognition and applications*, New Jersey, 1982.

[44] Mandelbrot B. Benoit, *The Fractal Geometry of Nature*, Macmillan, 1983.

[45] Daniel B, "Principal direction divisive partitioning," *Data Mining and Knowledge Discovery*, vol. 2, no. 4, pp. 325–344, December 1998.

[46] Michal D and Libor M, *Iris Database*, http://www.inf.upol.cz/iris/.

[47] CASIA, *Chinese Academy of Sciences Institute of Automation (CASIA)*, http://www.cbsr.ia.ac.cn/IrisDatabase".

[48] Arun R and Samir S, "Segmenting non-ideal irises using geodesic active contours," in *Biometric Consortium Conference*, September 2006, pp. 1–6.

[49] W.Y. Ma and B.S. Manjunath, "Edge flow: A framework of boundary detection and image segmentation," in *Computer Vision and Pattern Recognition, 1997. Proceedings., 1997 IEEE Computer Society Conference on*, June 1997, 17-19, pp. 744–749.

[50] K. Mathew Monaco, "Color space analysis for iris recognition," M.S. thesis, West Virginia University, 2007.

[51] R.D. Dony and S. Wesolkowski, "Edge detection on color images using rgb vector angles," in *Electrical and Computer Engineering, 1999 IEEE Canadian Conference on*, 1999, vol. 2, pp. 687–692.

[52] L David, "Distinctive image features from scale invariant keypoints," *International Journal of Computer Vision*, vol. 60, no. 2, pp. 91–110, November 2004.

[53] T. Lindeberg, "Scale-space theory: A basic tool for analysing structures at different scales," *Journal of Applied Statistics*, vol. 21, no. 2, pp. 224–270, 1994.

[54] K. Mikolajczyk, *Detection of Local Features invariant to affine transformations*, Ph.d.thesis, Institut National Polytechnic de Grenoble, France, 2002.

[55] T Lindeberg, "Feature detection with automatic scale selection," *International Journal of Computer Vision*, vol. 30, no. 2, pp. 77–116, 1998.

[56] Y Li, S David, and K Wang, "The relative distance of keypoint based iris recognition," *Pattern Recognition*, vol. 40, no. 2, pp. 423–430, 2007.